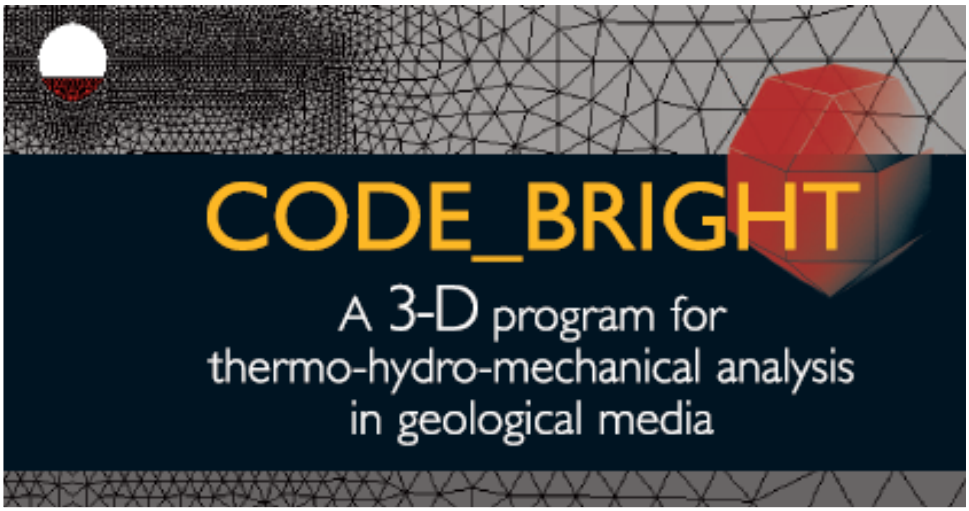
Workshop of
CODE_BRIGHT USERS

4 June 2025
Barcelona, Spain

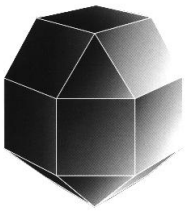


Department of Civil and Environmental Engineering
UPC-BarcelonaTech
Barcelona, Spain

CIMNE
International Center for Numerical Methods in Engineering
Barcelona, Spain

CODE_BRIGHT

A 3-D program for thermo-hydro-mechanical analysis in geological media



WORKSHOP OF CODE_BRIGHT USERS

Barcelona, 4 June 2025

Department of Civil and Environmental Engineering

(UPC-BarcelonaTech, Barcelona, Spain)

CIMNE

(International Center for Numerical Methods in Engineering, Barcelona, Spain)

CONTENTS

Numerical modeling of buoyancy effects in geological CO_2 storage
H. Wu, S. De Simone, V. Vilarrasa

Numerical modelling of soil-reinforcement interface with Mohr-Coulomb plasticity
S. Xiao, I.P. Damians

Numerical modelling of polyester strap reinforcements creep response
A. Moncada, I.P. Damians, S. Olivella, R.J. Bathurst

Analysis of surface settlements induced by construction of tunnels in urban areas including jet grouting umbrellas
E. Toprak, E. Alonso, S. Olivella

Modeling Rainfall-Induced Slope Failure with CODE_BRIGHT
A. Rodriguez-Dono, E. Badakshan, M. Buitrago, F. Song, Y. Wei, S. Olivella, J. Vaunat, A. Priegue, S.Valero, O. Fruitos

Coupled flow-deformation processes associated with the removal of root water uptake
C. Walker, A. Heitor, F. Loveridge, J. West, J. Gaucher, M. Smith

Thermal analysis of the Full-Scale In-Situ System Test (FISST) in Finland. Rock thermal properties
X. Pintado, T. Leino, M. Niskanen

Simulation of THM processes for a generic HLW repository
M. Hinze, L. Friedenberg

Insights into the daily life of a numerical modeler –an exemplary crushed salt modeling task
L. Friedenberg

NUMERICAL MODELING OF BUOYANCY EFFECTS IN GEOLOGICAL CO_2 STORAGE

Haiqing Wu[*,†], Silvia De Simone[††], Victor Vilarrasa[†]

[†] Global Change Research Group (GCRG), IMEDEA, CSIC-UIB, Esporles, Spain
[††] Institute of Environmental Assessment and Water Research (IDAEA), Spanish National Research Council (CSIC), Barcelona, Spain
[*] Corresponding author e-mail: Email: haiqing.wu@csic.es, now at Institute of Environmental Assessment and Water Research (IDAEA), Spanish National Research Council (CSIC), Barcelona, Spain

Key words: Buoyancy effects; fault stability; CO_2 storage

Abstract. *Upscaling CO_2 storage to the gigatonne scale may increase the potential of fault instability and thus induced seismicity. CO_2 is lighter than the resident brine by almost a factor of 2 under the pressure and temperature conditions of deep storage formations, which implies significant buoyancy effects during and after CO_2 injection. Here, we apply a numerical model to study the buoyancy effects of CO_2 on pore pressure diffusion, poromechanical response, and thus, fault stability. We consider a basin-scale model to meet the requirement of large-scale CO_2 storage. Simulation results highlight that buoyancy effects play a significantly role on the distribution of the CO_2 plume and poroelastic stress, while the values are quite similar between the cases with and without buoyancy effects. As a consequence, buoyancy effects slightly destabilize faults located below the CO_2 plume. This finding would be helpful to promote safe deployment of geological CO_2 storage projects.*

1 INTRODUCTION

Geological carbon storage has been proven to be an essential technology to reach net-zero carbon emissions to mitigate global climate change. CO_2 storage is being scaled up from the current level of tens of Mt per year to the gigatonne (Gt) level per year[i,ii]. Injecting a great amount of CO_2 into target formations at depth will lead to an extensive pore pressure diffusion and poromechanical response in the entire storage basin. In the past few decades, considerable studies have been focused on CO_2 diffusion, transport, and the poromechanical response of the subsurface during and after injection[iii-v], while not much attention was paid to the buoyancy effects of CO_2 on geomechanical stability.

CO_2 density ranges from 550 to 760 kg/m^3 at the general conditions of target formations[vi], which is, in average, about half of the density of the original resident brine. Such difference in density leads to gravity override of the CO_2 plume[vii]. However, how such buoyancy effects impact the poromechanical response and fault stability as well as the potential of induced seismicity has not been reported yet. To this end, this work aims at filling this knowledge gap by numerical modeling the buoyancy effects of CO_2 in geological CO_2 storage.

2 METHOD

We apply CODE_BRIGHT[viii,ix] to simulate the multiphase flow and fully coupled hydro-mechanical processes activated by the injection of CO_2 into a reservoir, with the final aim of studying the buoyancy effects of CO_2, i.e., the effects driven by the density difference between the resident brine and the lighter injected CO_2. We consider a basin-scale, 3D axisymmetric model containing six layers of an offshore storage site (Figure 1), which are assumed as

homogeneous, isotropic, and horizontal. The left side of domain represents the axis of axial symmetry. We assume the outer boundary conditions as constant pressure for the hydraulic problem to mimic an open reservoir system. We use elastic constitutive law to simulate the poromechanical response of the rock due to CO_2 injection. The van Genuchten model and a generalized power law model are adopted to represent the retention curve and the relative permeability curves of each phase, respectively. We impose mechanical boundary conditions of zero normal displacement on the right-lateral and lower boundaries and an overburden of -1.1 MPa on the upper boundary to mimic the load of 100 m seawater.

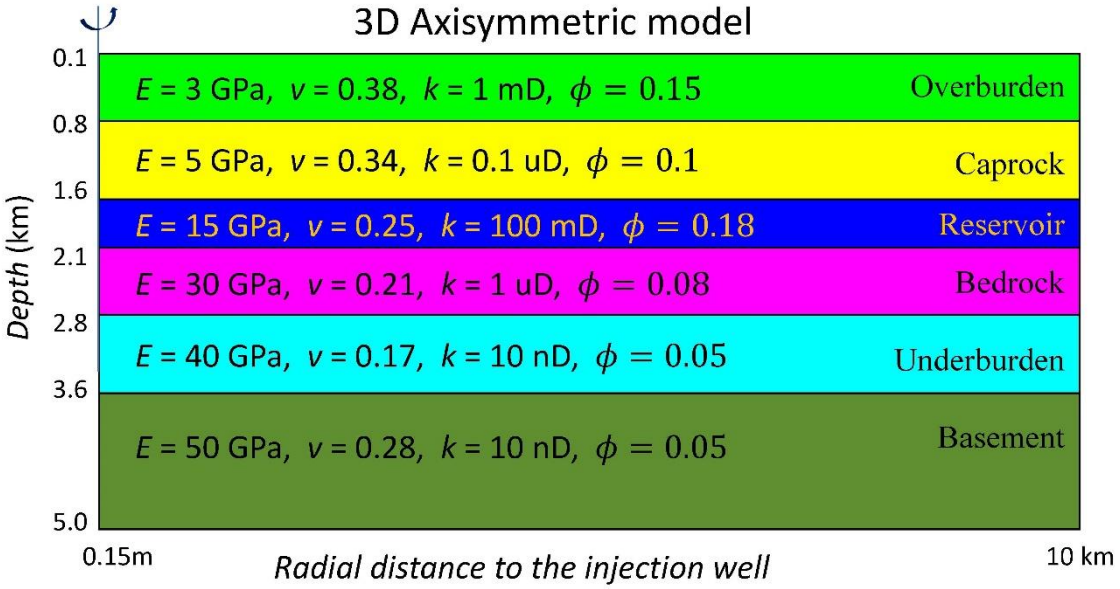


Figure 1: 3D axisymmetric model and geological setting of numerical simulations with CODE_BRIGHT. The value of rock properties for all geological layers is included, in which E and v denote Young's modulus and Poisson's ratio, respectively, k and ϕ represent the intrinsic permeability and porosity, respectively. The radius of the injection well is 0.15 m.

We continuously inject 1 Mt/yr of CO_2 at the well (left side of the model) for 60 years while we simulate a total period of 100 years. The injection is performed directly into the reservoir formation. We perform two simulations to analyze the buoyancy effects of CO_2: (1) one regular coupled poromechanical simulation which includes gravity effects and (2) one coupled poromechanical simulation in which gravity is set to zero. The difference between the simulations (1) and (2) illustrates the buoyancy effects of CO_2 due to the difference of its density compared to that of brine.

Once we have the simulated results of pore pressure and poroelastic stress at any instants of time from CODE_BRIGHT, we estimate fault stability by means of Coulomb Failure Stress $(CFS)^x$, assuming an inclined fault with a dip angle of 60° that could be placed at any locations of the simulation domain,

$$CFS = |\tau| - f_{st}(\sigma_n - p), \quad (1)$$

where σ_n and τ are the normal and shear stress components acting on the fault, respectively, f_{st} is the static friction coefficient of the fault, and p is the pore pressure. A positive value of CFS means an unstable fault and a negative value means a stable fault. Fault stability changes at an arbitrary instant of time are represented by Coulomb Failure Stress changes (ΔCFS) compared to its initial state

$$\Delta CFS = |\tau_t| - |\tau_0| - f_{st}(\Delta\sigma_n - \Delta p). \quad (2)$$

Similarly, a positive value of ΔCFS indicates a less stable fault and a negative value indicates a more stable fault.

3 RESULTS

In the regular simulation, after 30 years of injection, CO_2 penetrates into the target formation up to a distance of 2 km. Because CO_2 is lighter than brine, it floats on top of the brine and displaces into the target formation with a tendency to occupy the upper zone, creating the characteristic plume of curved inverted cone geometry (Figures 2a and 2c). In contrast, in the no-gravity simulation, i.e., neglecting gravity effects, CO_2 displaces with a piston-like front up to a distance smaller than 1 km (Figures 2b and 2d). While the shape of the CO_2 plume is different between the simulations, the CO_2 density is similar, with the maximum density being about 600 kg/m^3.

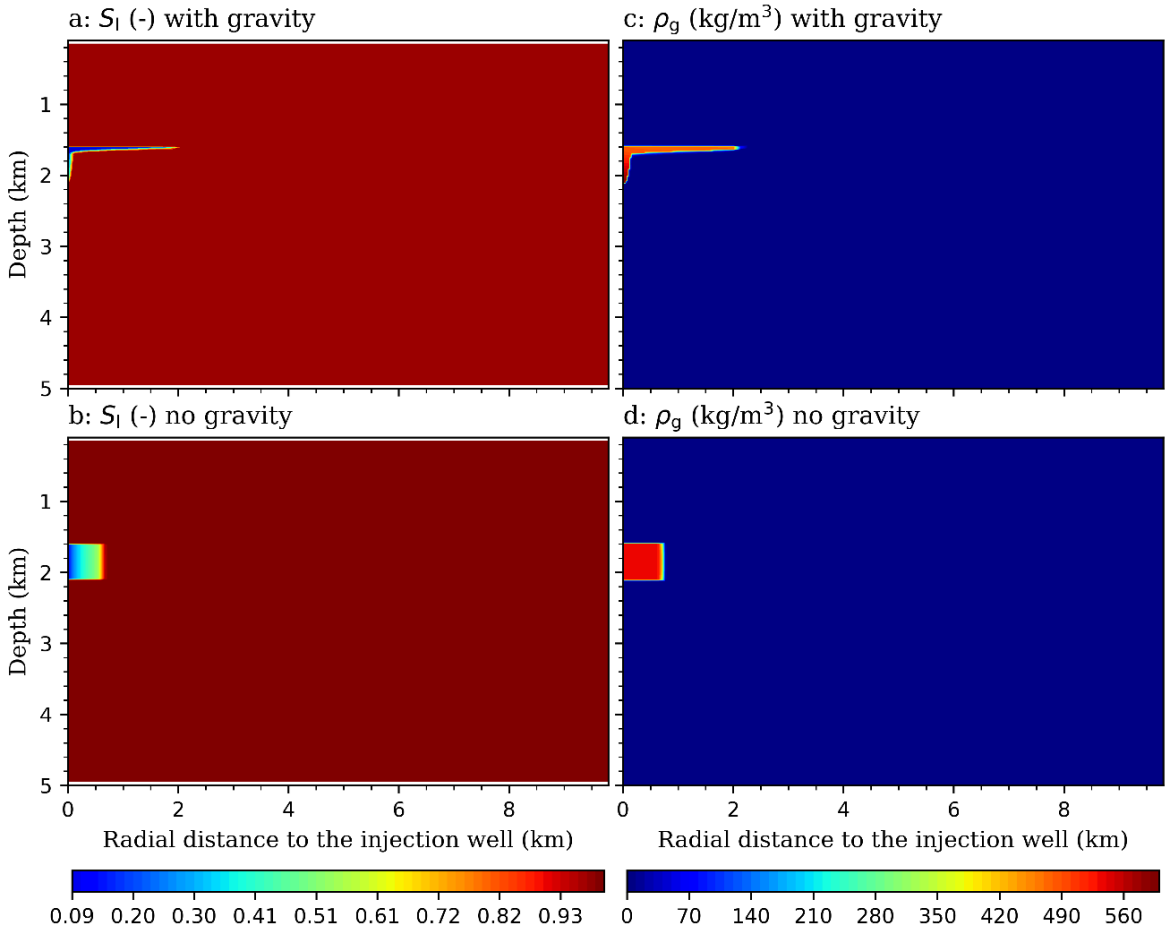


Figure 2: Distribution of (a and b) liquid saturation and (c and d) CO_2 density of the 3D axisymmetric model (a and c) with and (b and d) without gravity at the 30th year.

In both gravity and no-gravity cases, the axisymmetric geometry provokes compression and an increase of the total horizontal stress in the reservoir (Figures 3a and 3d). However, the total horizontal stress slightly decreases below the reservoir as a result of poroelastic response causing a decompression in this zone. This phenomenon is more evident in the gravity case. The variations of total vertical and shear stress components are instead small, but particularly interesting within the zone of the CO_2 plume and below it when comparing the gravity and no-

gravity cases (Figures 3b, 3c, 3e, and 3f). Because of buoyancy in the storage formation, the layers below it undergo an unloading with the total vertical stress decreasing.

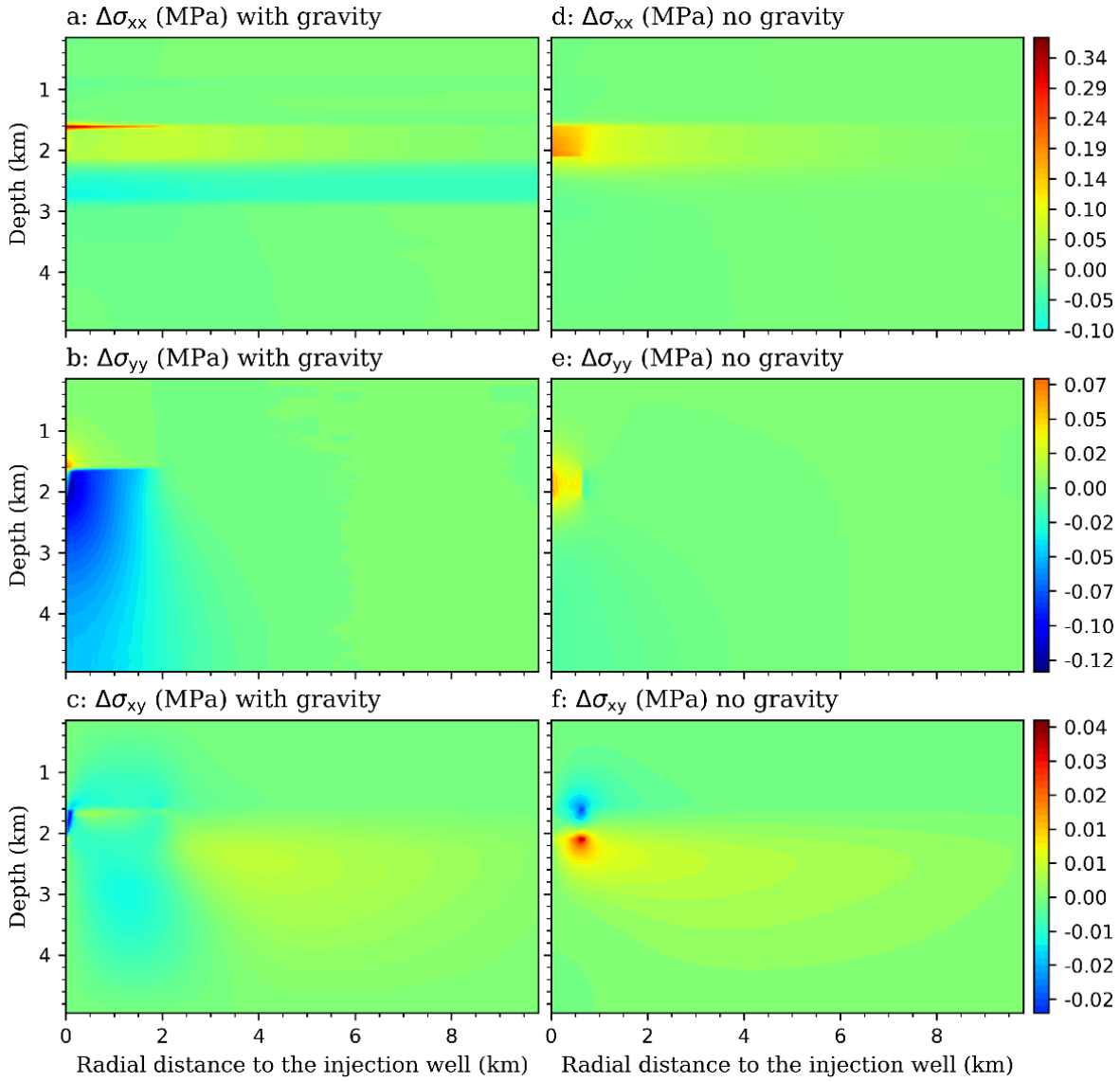


Figure 3: Distribution of poroelastic stress variations of (a and d) the horizontal, (b and d) the vertical, and (c and f) the shear components of the 3D axisymmetric model with (a, b, and c) and without (d, e, and f) gravity at the 30th year.

The variations of pressure and total stresses directly impact the effective stresses and therefore the changes in fault stability. We evaluate fault stability changes along the vertical line at a horizontal distance of 0.5 km away from the injection well to see how the buoyancy effects impact fault stability (Figure 4). In general, fault stability changes are quite small compared to the pore pressure changes because of the poromechanical response. For the regular simulation case considering gravity, ΔCFS is positive (which destabilizes faults) in the reservoir area occupied by CO_2 as well as its overburden, and it is negative (which stabilizes faults) in the reservoir zone outside the CO_2 plume and the underburden below the CO_2 plume (Figure 4b). The distribution of ΔCFS in the no-gravity simulation case is similar to that in the regular case, while the values are almost positive along this vertical line (Figure 4b). This is a

consequence of pore pressure changes (Figure 4a) and compression/decompression mechanisms induced by coupled poroelastic response and buoyancy effects (Figure 3). The difference in ΔCFS between the two cases implies that buoyancy effects slightly destabilize the fault located below the CO_2 plume.

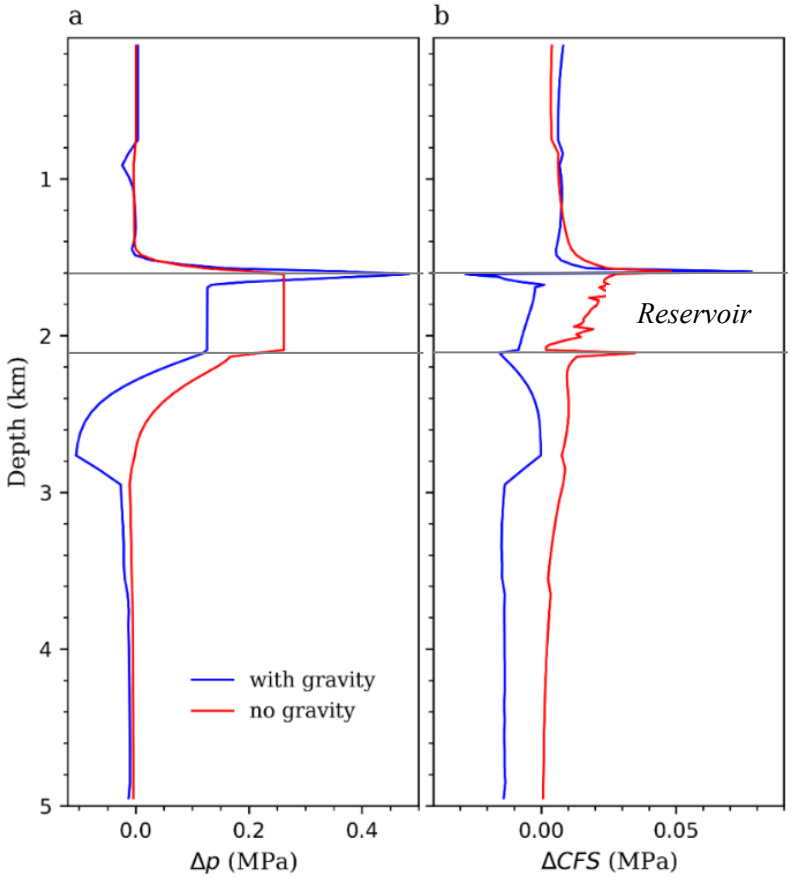


Figure 4: (a) Pore pressure changes and (b) Coulomb Failure Stress changes (ΔCFS) as a function of depth along the vertical line at r = 0.5 km of the 3D axisymmetric model at the 30th year. Horizontal gray lines indicate the top and bottom boundaries of the reservoir.

4 CONCLUSIONS

We study the buoyancy effects by comparing two simulations of CO_2 injection into the reservoir: one regular case acknowledging gravity and another neglecting gravity. Results highlight that buoyancy effects play a significantly role on the distribution of the CO_2 plume and poroelastic stress, while the poromechanical changes are quite similar between the two cases. We find that buoyancy effects may slightly destabilize faults located below the CO_2 plume.

ACKNOWLEDGMENTS

The authors acknowledge the support from Repsol. IMEDEA is an accredited “Maria de Maeztu Excellence Unit” (Grant CEX2021-001198, funded by MCIN/AEI/10.13039/501100011033). S.D.S. acknowledges the support of the ‘Ramón y Cajal’ fellowship (reference RYC2021-032780-I) funded by MICIU /AEI /10.13039/501100011033 and by "European Union Next Generation EU/PRTR".

REFERENCES

[i] Global CCS Institute (2019). The Global Status of CCS 2019: Targeting Climate Change. Australia.

[ii] Global CCS Institute (2024). The Global Status of CCS 2024: Collaborating for a Net-Zero Future.

[iii] Cheng, Y., Liu, W., Xu, T., Zhang, Y., Zhang, X., Xing, Y., Feng, B. and Xia, Y., 2023. Seismicity induced by geological CO_2 storage: A review. Earth-Science Reviews, 239, p.104369.

[iv] Song, Y., Jun, S., Na, Y., Kim, K., Jang, Y. and Wang, J., 2023. Geomechanical challenges during geological CO_2 storage: A review. Chemical Engineering Journal, 456, p.140968.

[v] Narayanan, S.Y. and Singh, D.N., 2025. Geological storage of CO2 in deep saline sandstone aquifers: A geomechanical perspective. Journal of Rock Mechanics and Geotechnical Engineering.

[vi] Onyebuchi, V.E., Kolios, A., Hanak, D.P., Biliyok, C. and Manovic, V., 2018. A systematic review of key challenges of CO2 transport via pipelines. Renewable and Sustainable Energy Reviews, 81, pp.2563-2583.

[vii] Vilarrasa, V., Makhnenko, R. and Gheibi, S., 2016. Geomechanical analysis of the influence of CO_2 injection location on fault stability. Journal of Rock Mechanics and Geotechnical Engineering, 8(6), pp.805-818.

[viii] Olivella, S., Carrera, J., Gens, A., & Alonso, E. E., 1994. Non-isothermal Multiphase Flow of Brine and Gas through Saline media. Transport in Porous Media, 15, 271:293

[ix] Olivella, S., Gens, A., Carrera, J., & Alonso, E. E., 1996, 'Numerical Formulation for a Simulator (CODE_BRIGHT) for the Coupled Analysis of Saline Media " Engineering Computations, Vol 13, No 7, pp: 87-112.

[x] King, G. C., Stein, R. S., & Lin, J. (1994). Static stress changes and the triggering of earthquakes. Bulletin of the Seismological Society of America, 84(3), 935-953.

NUMERICAL MODELLING OF SOIL-REINFORCEMENT INTERFACE WITH MOHR-COULOMB PLASTICITY

Shuxiong Xiao[*] and Ivan P. Damians[*†]

[*] Department of Civil and Environmental Engineering, Universitat Politècnica de Catalunya, Barcelona, Spain
[†] International Centre for Numerical Methods in Engineering (CIMNE), Barcelona, Spain
E-mail: shuxiong.xiao@upc.edu

Key words: Numerical modelling, soil-reinforcement, interface, direct shear

Abstract. *The soil-reinforcement interaction issue is commonly encountered in the design of reinforced soil walls (RSWs). Direct shear test is a fundamental laboratory approach to study interfacial behaviour between soil and reinforcement. Therefore, we propose a 2D numerical modelling of direct shear test regarding soil-reinforcement interface. The interface zone is characterized as linear elastic material with Mohr-Coulomb (M-C) plasticity, and a simple calibration method is presented. Comparison between reported data and simulation result indicates the M-C law generally performs well, yet shear strength overestimation occurs when volume change is not allowed.*

1 INTRODUCTION

Reinforcement elements (typically steel- or polymeric-based) have played an important role in the design of reinforced soil walls (RSWs). One fundamental approach for studying soil-reinforcement interaction mechanism is direct shear test, which has a simple set-up, low cost and can provide straightforward shear strength and stiffness parameters for the optimization of RSWs design.

So far, experimental studies[i,ii] and numerical simulations[iii,iv] regarding soil-reinforcement interface has been widely reported, focusing on soil/reinforcement types, confining conditions or initial states. However, in their simulations the constitutive model used is usually complicated, requiring up to a dozen -parameters with unclear physical meanings. Therefore, we propose a numerical simulation of soil-reinforcement direct shear test using Mohr-Coulomb plasticity, which is simpler and more practicable. Reported testing data is also used to examine the performance of the interface methodology with Mohr-Coulomb law in the simulation of direct shear test.

2 NUMERICAL MODELLING

2D numerical model for direct shear test was established in the finite element software Code_bright[v], as shown in Fig. 1. In the model, the upper shear box is filled with soil, beneath the soil lays the reinforcement which is glued by the steel block. Interface zone between soil and reinforcement was modelled as a linear elastic material with Mohr-Coulomb plastic, while soil, reinforcement and steel were assumed behaving linear elastic, because of the dominant role interface playing in the behaviour of the system.

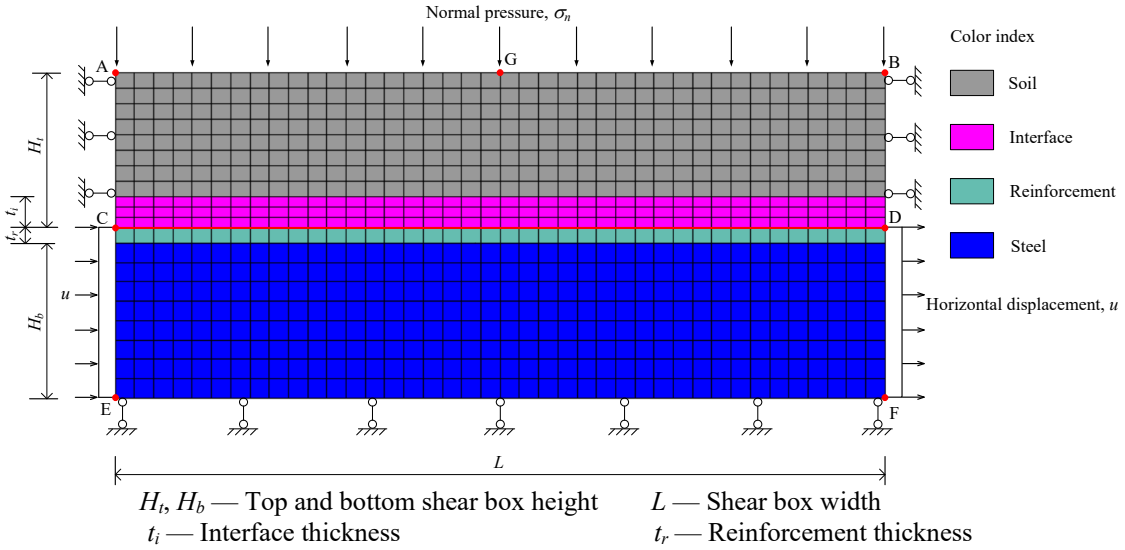


Fig. 1. Numerical model of soil-reinforcement direct shear test in Code_bright.

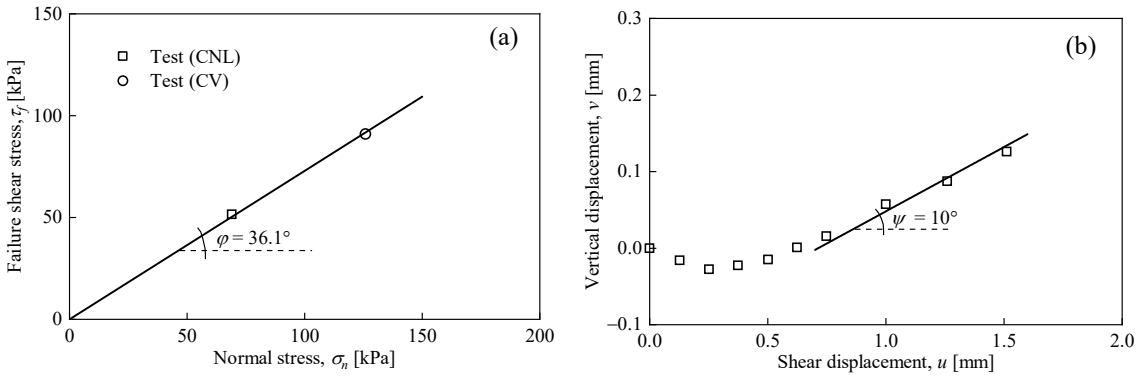
Two loading paths were considered in the simulation, namely, constant normal load (CNL) and constant volume (CV). The boundary condition shown in Fig.1 corresponds to CNL path, which can be changed to CV scenario by simply replacing the top boundary from a constant stress to a fixed vertical displacement. The simulation process was split into pressurizing stage and shear stage.

3 CALIBRATION AND VALIDATION

3.1 Calibration of interface parameters

As the interface is assumed linear elastic with M-C plasticity, 5 constitutive parameters: Young's modulus E, Poisson's ratio μ, cohesion c, friction angle φ and dilatancy angle ψ, are required for the numerical simulation. The geometric thickness of the interface, t_i, is selected in the range of 5-10 times mean particle size (d_{50}).

Fig. 2 gives a schematic procedure for calibrating the interface parameters, from the measured shear stress- and vertical displacement-shear displacement data of the direct shear test[vi]. This is reasonable because we attribute the system performance into the interface behaviour. Note that this calibration method is no longer applicable when considering the soil plasticity (here the soil is assumed elastic).



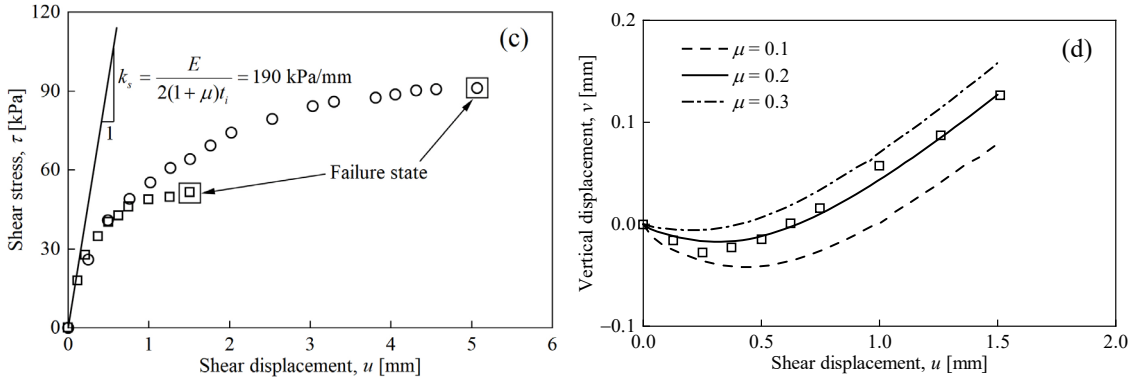


Fig. 2. Calibration of soil-reinforcement interface parameters: (a) friction angle φ, (b) dilatancy angle ψ, (c) Young's modulus E, and (d) Poisson's ratio μ. (data from sand-steel interface test[vi])

3.2 Validation and discussion

Direct shear tests on sand-steel interface[vi] and sand-woven geotextile interface[vii] are used to validate the proposed numerical method, corresponding to stiff and soft reinforcement materical respectively.

Fig. 3 shows the comparison between the computed and measured results of sand-steel interface test, where both CNL and CV loading path are incorporated. As shown in Fig. 3, good consistency between model predictions and testing data is observed, indicating the Mohr-Coulomb generally performs well in simulating interface, yet obvious deviation occurs in the CV case. This may be attributed to the constant dilation angle assumption of M-C law.

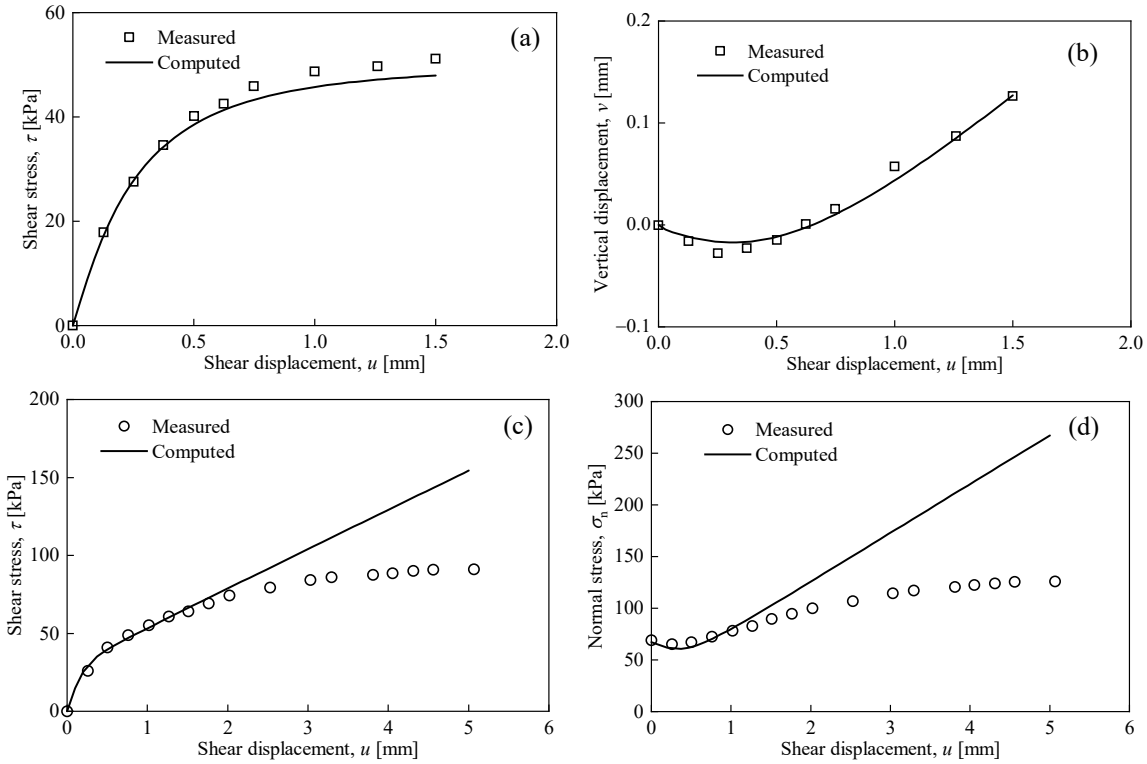


Fig. 3. Computed results against measured data of sand-steel interface direct shear test: (a-b) constant normal load (CNL) path; (c-d) constant volume (CV) path (data from sand-steel interface test[vi])

The second simulation case is the sand-woven geotextile interface test, in which different normal pressures (σ_n = 57, 107 and 207 kPa) are applied, as shown in Fig. 4. Overall, good agreement between numerical computations and experimental observations is obtained, and the increase of shear strength as well as decrease of dilatative deformation with normal pressure can be well captured by the M-C plastic law.

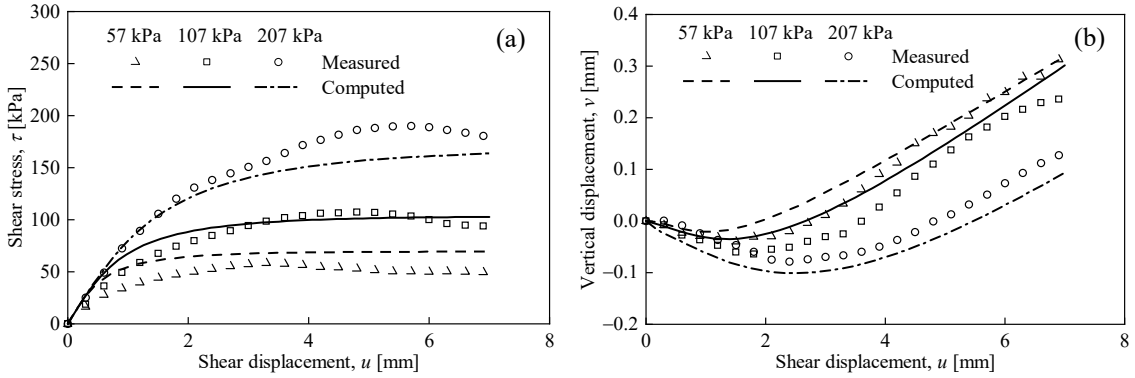


Fig. 4. Computed results against measured data of sand-woven geotextile interface direct shear test: (a) shear stress evolution and (b) vertical displacement evolution (data from sand-woven geotextile interface test[vii])

4 CONCLUSIONS

We present a 2D numerical modelling of direct shear test on soil-reinforcement interface, with use of M-C failure criterion. Two sets of reported testing data is used to examine the performance of the M-C law in simulating soil-reinforcement interface. The main conclusions are addressed as follows:

(1) The overall good agreement between computed results and measured data is reached, validating the capacity of M-C plasticity in simulating soil-reinforcement interface.

(2) It's revealed that the M-C plasticity performs well when different loading pressures are involved, yet overestimation of shear strength under constant volume condition is unavoidable.

(3) The proposed method fails to consider strain softening and soil plasticity, improvement should be made to give a more realistic simulation.

REFERENCES

[i] Lashkari, A., Jamali V., 2021. Global and local sand-geosynthetic interface behaviour. Géotechnique, 71(4): 346-367.

[ii] DeJong, J. T., Westgate, Z. J., 2009. Role of initial state, material properties, and confinement condition on local and global soil-structure interface behavior. J. Geotech. Geoenviron. Eng., 135(11): 1646-1660.

[iii] Hu, L., Pu, J. L., 2003. Application of damage model for soil-structure interface. Comput. Geotech., 30(2): 165-183.

[iv] Saberi, M., Annan, C. D., Konrad, J. M., 2019. Implementation of a soil-structure interface constitutive model for application in geo-structures. Soil. Dyn. Earthq. Eng., 116: 714-731.

[v] Olivella, S., A. Gens, J. Carrera, E. E. Alonso, 1996, 'Numerical Formulation for a Simulator (CODE_BRIGHT) for the Coupled Analysis of Saline Media " Engineering

Computations, Vol 13, No 7, pp: 87-112.
[vi] Zeghal, M., Edil, T. B., 2002. Soil structure interaction analysis: modeling the interface. Can. Geotech. J., 39(3): 620-628.
[vii] Afzali-Nejad, A., Lashkari, A., Shourijeh, P. T., 2017. Influence of particle shape on the shear strength and dilation of sand-woven geotextile interfaces. Geotext. Geomembr, 45(1): 54-66.

NUMERICAL MODELLING OF POLYESTER STRAP REINFORCEMENTS CREEP RESPONSE

A. Moncada[*†], I.P. Damians[*†‡], S. Olivella[*†] and R.J. Bathurst[§]

[*] Department of Civil and Environmental Engineering (DECA), Universitat Poliècnica de Catalunya (UPC), Campus Nord UPC, 08034 Barcelona, Spain.
e-mail: anibal.moncada@upc.edu

† International Centre for Numerical Methods in Engineering (CIMNE), Campus Nord UPC, 08034 Barcelona, Spain. (http://www.cimne.com)

‡ VSL International Ltd, Barcelona, Spain

§ Geoengineering Centre at Queen's-RMC, Civil Engineering Department, Royal Military College of Canada, Canada.

Key words: Coupled constitutive model, geosynthetics, creep, reinforced soil, CODE_BRIGHT.

Abstract. *The response of geosynthetic materials have been shown to vary depending on the conditions to which they are subjected (i.e., load, time, and temperature). The present work details the formulation, validation and implementation of a viscoplastic constitutive model with coupled dependencies aimed to simulate the long-term response of polymeric material, particularly that of polyester strap reinforcements. The model is aimed at predicting primary and secondary creep. For calibration, a wide data-set of polyester strap reinforcement creep measurements was used. The validation process was done using parameters for load-, product-, and material-specific scenarios. Load- and product-specific scenarios showed suitable agreement between simulated and measured data. The coupled capabilities of the model are shown via idealized temperature and relative humidity boundary conditions. Simulations of stress-relaxation response for constant rate of strain scenarios are also provided. The proposed formulation is aimed at modelling the long-term response of reinforced soil structures while accounting for the effect of in-air or in-soil conditions to which reinforcement materials can be exposed to throughout the structure's life-cycle.*

1 INTRODUCTION

Polyester (PET) strap reinforcements are commonly used in reinforced soil walls (Figure 1a), where reinforcement elements, perpendicular to the main stress direction, act as stress bearing components (Figure 1b). PET strap reinforcements work as a compound material, combining the response of the PET fibres, which act as the load-bearing component, and a covering sheath, that serves as a protective component (Figure 1c). The composite nature of reinforcements is an added difficulty when predicting its behaviour, as there will be a micro- and macro-structural response. As load increases, fibres are tensioned, adjustment between the fibres and the sheath can occur, as well as between the sheath and the soil (in the case of a structure) or clamps (in the case of laboratory). The focus of this work is the macro response of the material.

The long-term response of extensible geosynthetic materials[i] depends on several mechanism

that can change with the conditions to which the materials are exposed to[ii].

In analytical design methods, structures with polymeric reinforcements reduce the characteristic tensile strength to account for these mechanisms with material factors, which include installation damage, chemical weathering, environmental degradation, creep deformation, and an uncertainty factor[iii]. All partial factor must be obtained based on laboratory testing. If no data is available, conservative values obtained in the literature could prove useful.

In numerical models, polymeric reinforcements are usually characterized using a single stiffness value. The response of geosynthetic materials has been proven to be load-, time-, and temperature-dependent, thus, the selection of a unique stiffness value can be difficult. An accepted method to select a single stiffness value is the use of isochronous strain-stiffness curves, based on a strain (e.g., 2%) and time (e.g., 1000 hours) criteria[iv]. Another approach is the use of tailor-made constitutive laws for geosynthetic materials. Numerous formulations for the short- and long-term response of geosynthetic materials can be found in the literature[v,vi,vii].

The present study is based on the authors' previous work[viii] and focuses on the development of a coupled viscoplastic constitutive formulation to simulate the long-term response of PET strap reinforcements with varying sheath materials. Model calibration was undergone using laboratory creep measurements obtained using the SIM. Following this, the model was implemented in a finite element software and tested for idealized scenarios.

2 FORMULATION

The proposed model consists of a combined linear elastic and viscoplastic approach based on viscoplasticity theory, aimed at the creep deformation of structural materials. Stress and strain tensors are described in cartesian coordinates and, for each component, denoted by the subscript ij (i.e., ij = xx, yy, zz, xy, xz, and yz). The stress and strain tensors include longitudinal (e.g., σ_{xx} and ε_{xx}) and shear (e.g., σ_{xy} and ε_{xy}) components. For an isotropic, homogeneous material, total strains for a given component (ε_{ij}) are the sum of an elastic (ε_{ij}^{e}) and viscoplastic

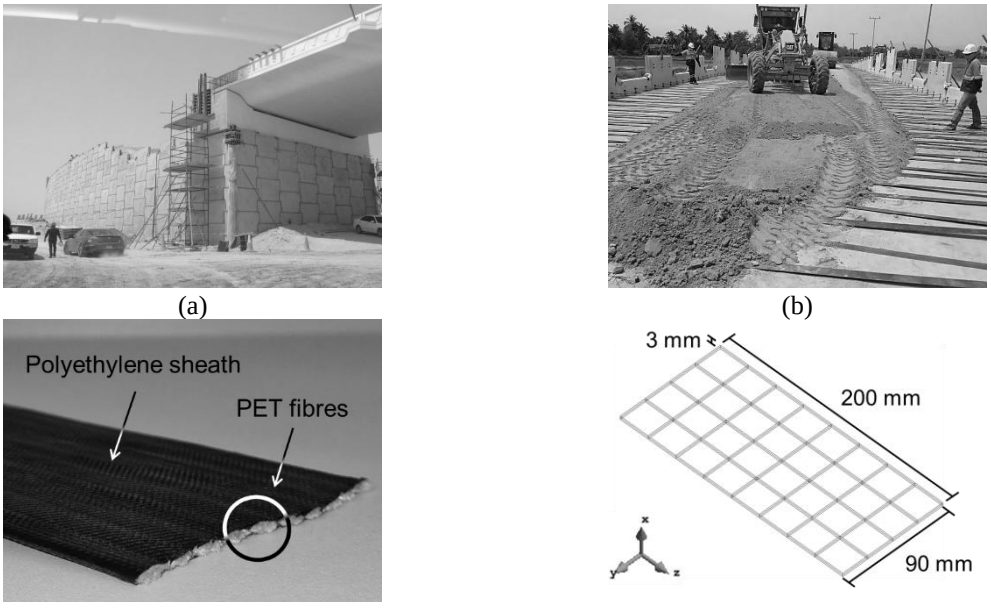


Figure 1. Details of a (a) PET strap reinforcement (courtesy of GECO Industrial), (b) reinforced soil wall bridge abutment, (c) reinforced soil wall with PET straps reinforcements under construction. (courtesy of VSL International Ltd.), and (d) finite element mesh geometry (adapted from [viii]).

(ε_{ij}^{vp}) components. Elastic strains are defined by a linear elastic Young's modulus (E) and Poison's ratio (ν). Viscoplastic strains are time-dependent (Eq. 1), where the rate of viscoplastic strain ($\dot{\varepsilon_{ij}}^{vp}$), also understood as the rate of creep, is formulated using Perzyna's overstress theory[ix]. The plastic component of the strain tensor at any direction will be a function of the excess stresses above the yield function F (Eq. 2). For in-air, axial stress conditions, strains are given by the longitudinal direction and the shear component is not overly relevant. On the contrary, for an embedded, in-soil reinforcement, the shear component is crucial, as stress transfer mechanism of the soil-reinforcement interaction is through shear.

$$\varepsilon_{ij}^{vp} = \int_0^t \dot{\varepsilon}_{ij}{}^{vp} dt \tag{1}$$

$$\dot{\varepsilon}_{ij}{}^{vp} = \gamma\, F^n \frac{\partial F}{\partial \sigma'_{ij}} \tag{2}$$

Here, t is time (in s), γ is a fluidity parameter (in s/Mpa^n), F is a yield function of stress (in Mpa), given by a von-Mises type surface (i.e., deviatoric stress, q) (also used by Eldesouky and Brachman[x], who obtained excellent results simulating HDPE geomembranes), and n is a power parameter (-). A value of n = 6 was found to properly fit the test data. For uniaxial test conditions, say, in direction y, the deviatoric stress q matches the axial stress σ_{yy}. The described model focuses on the fluidity parameter in a similar manner as a hardening parameter. The fluidity parameter is defined by two components, which account for primary ($\dot{\varepsilon}_{ij\,primary}^{vp}$) and secondary ($\dot{\varepsilon}_{ij\,secondary}^{vp}$) (Eq. 4). Primary creep is defined by a decreasing rate of viscoplastic strain with time, while secondary creep corresponds to a constant rate of viscoplastic strain with time for a given stress state.

The two-component fluidity is defined by the sum of two functions, A and B, which account for primary and secondary creep, respectively. A is an exponential function of accumulated viscoplastic strains with two curve fitting parameters (A1 and A2), while B is proposed as a constant function for any given stress state. Being a thermally activated process[xi], the reaction rate of PET and other geosynthetic materials follow an Arrhenius formulation (Eq. 4)[xii]. Moreover, the hydrolytic response of PET filaments has a proportional dependency via a power function of relative humidity within the overall kinetics[xiii]**.** Accordingly, an Arrhenius type expression is added to the fluidity parameter. For a non-zero stress state (i.e., q > 0), the viscoplsatic rate of strain is given by a function of stress, strain, time, temperature, and relative humidity as expressed in Eq. 5.

$$\dot{\varepsilon}_{ij}{}^{vp} = \dot{\varepsilon}_{ij_{primary}}^{vp} + \dot{\varepsilon}_{ij_{secondary}}^{vp} \tag{3}$$

$$R = \alpha \exp\left(-\frac{Q}{RT}\right) \tag{4}$$

$$\dot{\varepsilon}_{ij}{}^{vp} = \gamma\left(\varepsilon_{ij}^{vp}, T, RH\right) F^n \frac{\partial F}{\partial \sigma'_{ij}} = \left[A_1 \exp\left(-A_2 \varepsilon_{ij}^{vp}\right) + B\right] \exp\left(-\frac{Q}{RT}\right) RH^m F^n \frac{\partial F}{\partial \sigma'_{ij}} \tag{5}$$

Here, RH is fractional relative humidity (-), m is a power parameter (-), Q is activation energy (in J/mol), R is the universal gas constant (in J/mol K), and T is temperature (in K). The activation energy, temperature and relative humidity dependencies could vary between mechanism (in this case primary and secondary creep). Due to a lack of laboratory data and for simplicity's sake, both mechanisms are considered to have the same dependencies of Q, T, and RH. The current work considers a constant Q value of 100 kJ/mol. For the relative humidity power function, a value of m = 2 was used. Regarding the stress power function,

3 NUMERICAL IMPLEMENTATION

The constitutive model was implemented in CODE_BRIGHT[xiv]. For this, a 3D PET strap specimen, 200-mm-long, 90-mm-wide, and 3-mm-thick, was modelled (Fig. 1d). As the present simulation does not include other materials (i.e., in-air simulations) thermal and hydraulic properties are not required.

Model calibration was done in three stages: a load-specific, a product-specific, and a material-wide scenario. Simulated results properly reproduce the creep response for the load- and product-specific cases. The material-wide scenario did not yield accurate results. For further details on the calibration process, please refer to the authors previous work[viii]

Figure 2a shows the effect of monotonic stress increments on the strain response with time. An initial load of 20% UTS is increased to 30% and 40% UTS, load range in which only primary creep is expected. The increase in load shifts the strain trajectory upwards, matching the modelled creep curves at each load condition.

For a fixed strain, viscoplastic strains developed over time requires for a negative rate of elastic strain, which results in a negative rate of stress, thus, allowing for stress-relaxation to occur. The rate of relaxation is related to the value of n (in the present study n= 6 was used). Higher n-values result in higher creep and relaxation rates. Figure 2b shows modelled results for controlled rate of strain tests (i.e., stress-relaxation results) for three initial strain values. Additionally, the figure shows data stress-relaxation results extracted from the work of Kaliakin and Bathurst[xv]. Initial stresses are reduced 26.5%, 12.7%, and 4.2%, for fixed strain values of 1.1%, 2.2%, and 5.5%, respectively, at 20ºC. Relaxation values appear to be on the low-end when compared to literature data of PET geogrids, but are deemed reasonable. The modelled stress-relaxation trajectory is rather linear with a continuous decrease in stress over time. Fig. 9b also shows stress-relaxation results at 10ºC and 30ºC considering a 2.2% fixed strain. Stress reduction varies from 10.6% at 10ºC to 14% at 30ºC, which can be understood as an increase in the ductility of the material as temperature increases.

Figure 2c shows the creep response of the numerical model for constant relative humidity conditions of 70% and 100% at 10ºC, 20ºC, and 40ºC for a constant load of 40% UTS. An increment of 30% in relative humidity values, which correspond to a liquid pressure variation of almost 50 MPa at 20ºC, increases the total strain by 5% (i.e., total strain increases from 6.01% to 6.05%) within 100 000 hours. These results should be taken as a tentative and idealized approach of what is a composite material response Temperature increments shift the creep curve upwards, increasing overall strains, while maintain a rather constant slope.

Figure 2d shows modelled creep results at a load of 40% UTS with a variable temperature boundary condition as well as the temperature time history at a constant relative humidity of 70%. For comparison purposes, creep results at 20ºC, 30ºC, and 35ºC are included. Note that the x-axis is not in log-scale. The temperature boundary condition simulates annual fluctuations with is a sine function, with an amplitude of 15ºC, mean value of 20ºC and a period of 365 days. As temperature decreases, the slope of the strain trajectory decreases, which can be seen as plateaus in the strain trajectory. As temperature increases, the rate of strains increases. Since the model is not elastic (i.e., long-term deformations are not recoverable), the rate of strain at lower temperatures does not compensate for the increase rate of strain at higher temperatures. Overall, a cyclic temperature boundary condition results in higher strain values than that of a sample at a constant 20ºC (equal to the boundary condition mean value), but slightly lower than that at 35ºC (lower than the boundary condition maximum value). Obtained results are encouraging as they evidence the applicability of the proposed model for constant and transient temperature conditions.

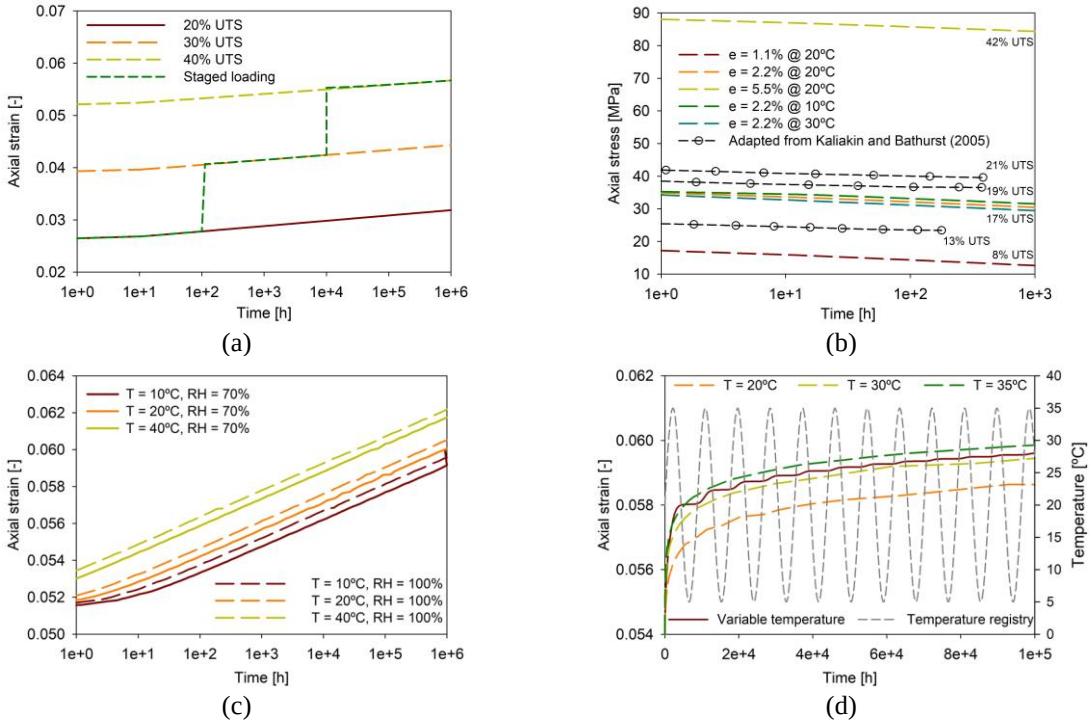


Figure 2. Finite element model results for (a) load variations (controlled rate of stress), (b) stress-relaxation (controlled rate of strains) scenarios, and, for a constant load of 40% UTS, (c) different relative humidity and temperature scenarios, and (d) variable temperature boundary conditions (adapted from [viii]).

4 CONCLUSIONS

- The paper describes the implementation of a coupled viscoplastic constitutive model to simulate the primary and secondary creep response of PET strap reinforcements.
- Model parameters were obtained by fitting creep curves, obtained via the steep isothermal method, available in the literature.
- The effect of temperature and relative humidity was explored. Higher temperatures increased creep strains with time. When considering cyclic temperature boundary conditions, temperature increments resulted in increased rate of strains, while lower temperatures resulted in the opposite. Due to lack of extensive data, results must be taken as idealized scenarios which show the capability of the model.
- Response under constant rate of strain conditions showed a decrease in stresses with time (i.e., stress-relaxation). Relaxation was more pronounced at lower strain values. As with creep, stress-relaxation rate depends on the exponent in the power function of stress.
- Future work is focused on the application of the proposed formulation in coupled numerical models of full-scale structures.

ACKNOWLEDGEMENTS

The authors wish to thank Dr. Richard J. Bathurst for the provided guidance and reliability data of various polymeric strap reinforcements and Aaron Kim from GECO Industrial (Korea, Rep) for providing data from reliability assessment testing records. The authors wish to acknowledge the support of the Department of Civil and Environmental Engineering (DECA) of the Universitat Politècnica de Catalunya·BarcelonaTech (UPC) and the International Centre for Numerical Methods in Engineering (CIMNE).

REFERENCES

[i] Miyata, Y., Bathurst, R.J., Allen, T.M., 2018. Evaluation of tensile load model accuracy for PET strap MSE walls. *Geosynth. Int*., 25(6), 656-671.

[ii] Koerner, R.M., Lord Jr, A.E., Halse, Y.H., 1988. Long-term durability and aging of geotextiles. *Geotext. and Geomembr*., 7(1-2), 147-158.

[iii] BS 8006-1: 2010 + A1, 2016. Code of practice for strengthened/reinforced soils and other fills. BSI, Milton Keynes, UK.

[iv] Allen, T.M., Bathurst, R.J., 2019. Geosynthetic reinforcement stiffness characterization for MSE wall design. *Geosynth. Int*., 26(6), 592-610.

[v] Zhang, C., Moore, I., 1997. Nonlinear mechanical response of high density polyethylene. Part I: experimental investigation and model evaluation. Polym. Eng. Sci. 37, 404–413

[vi] Kongkitkul, W., Tabsombut, W., Jaturapitakkul, C., Tatsuoka, F., 2012. Effects of temperature on the rupture strength and elastic stiffness of geogrids. Geosynth. Int., 19(2), 106-123.

[vii] Bathurst, R.J., Naftchali, F.M., 2021. Geosynthetic reinforcement stiffness for analytical and numerical modelling of reinforced soil structures. Geotext. and Geomembr., 49(4), 921-940

[viii] Moncada, A., Damians, I.P., Olivella, S., 2024. Thermo-hydro-mechanical viscoplastic constitutive model for polyester strap reinforcement long-term response. Computers and Geotech., 175, 106695.

[ix] Perzyna, P., 1966. Fundamental problems in viscoplasticity. Adv. in Appl. Mech., 9, 243-377.

[x] Eldesouky, H.M.G., Brachman, R.W.I., 2020. Viscoplastic modelling of HDPE geomembrane local stresses and strains. Geotext. and Geomembr., 48(1), 41-51.

[xi] Koerner, R.M., Lord Jr, A.E., Hsuan, Y.H., 1992. Arrhenius modeling to predict geosynthetic degradation. *Geotext. and Geomembr*., 11(2), 151-183.

[xii] Greenwood, J.H., Schroeder, H.F., Voskamp, W., 2012. Durability of Geosynthetics (Publication 243). CUR Committee C 187. Build. and Infrastruct. ISBN 978-90-376-0533-4.

[xiii] Pickett, J.E., Coyle, D.J., 2013. Hydrolysis kinetics of condensation polymers under humidity aging conditions. Polym. Degrad. and Stab., 98(7), 1311-1320.

[xiv] Olivella, S., A. Gens, J. Carrera, E.E. Alonso, 1996. Numerical Formulation for a Simulator (CODE_BRIGHT) for the Coupled Analysis of Saline Media. Eng. Comput., Vol 13, No 7, pp: 87-112.

[xv] Kaliakin, V.N., Bathurst, R.J., 2005. Review of numerical models for geosynthetics in reinforcement applications. In Computer Methods and Advances in Geomechanics: 11th Int. Conf. of the Int. Assoc. for Computer Methods and Advances in Geomech., Torino, Italy. 4, 407-416.

Analysis of Surface Settlements Induced by Construction of Tunnels in Urban Areas including Jet Grouting Umbrellas

Erdem Toprak[1], Eduardo Alonso[1,2] and Sebastia Olivella[1,2]

[1]International Centre for Numerical Methods in Engineering (CIMNE), Barcelona, Spain

[2]Department of Civil and Environmental Engineering, Universitat Politècnica de Catalunya, Barcelona, Spain

*mailto:erdem.toprak@upc.edu

Abstract. *Tunnels in urban areas for underground railway are usually shallow and cross low resistance materials. Horizontal jet grouting (HJG) is commonly used in tunnelling projects to improve ground stability and control settlements. This study focuses on the numerical modeling of the settlements caused by an urban tunnel excavation that includes HJG application, specifically when using the New Austrian Tunnelling Method (NATM). The advanced finite element software CODE_BRIGHT was employed to simulate the complex mechanical behavior of jet-grouted soils and to analyse the mechanisms behind rapid settlement. The results indicate that development of jet grouting umbrellas may induce significant volumetric deformations above the tunnel if not correctly implemented, resulting in substantial surface settlements. The study also highlights the limitations of using NATM in soft soils. The findings contribute to a better understanding of HJG applications and offer valuable insights for engineers working on urban tunnelling projects where jet grouting is required.*

Keywords: Horizontal jet grouting, urban tunnelling, surface settlements, CODE_BRIGHT.

1. Introduction

The New Austrian Tunneling Method (NATM) and Horizontal Jet Grouting (HJG) are widely utilized in tunneling projects due to their adaptability and proven effectiveness across diverse geotechnical conditions. However, their combined application in soft soil environments, particularly within densely developed urban areas, presents notable challenges related to ground deformation and overall tunnel stability. NATM is a deformation-controlled tunneling method that capitalizes on the inherent load-bearing capacity of the surrounding ground, enhanced through systematic monitoring and sequential support installation [i]. Nevertheless, when implemented in soft soil formations, significant concerns arise due to the low shear strength, high compressibility, and time-dependent behavior of these soils [ii].

This study presents a real-case application of HJG during an urban tunneling project. The model geometry (**Figure 1a**), the tunnel cross-section (**Figure 1b**) and construction sequence, following the NATM, are detailed in **Figure 1c** and **Figure 1d**.

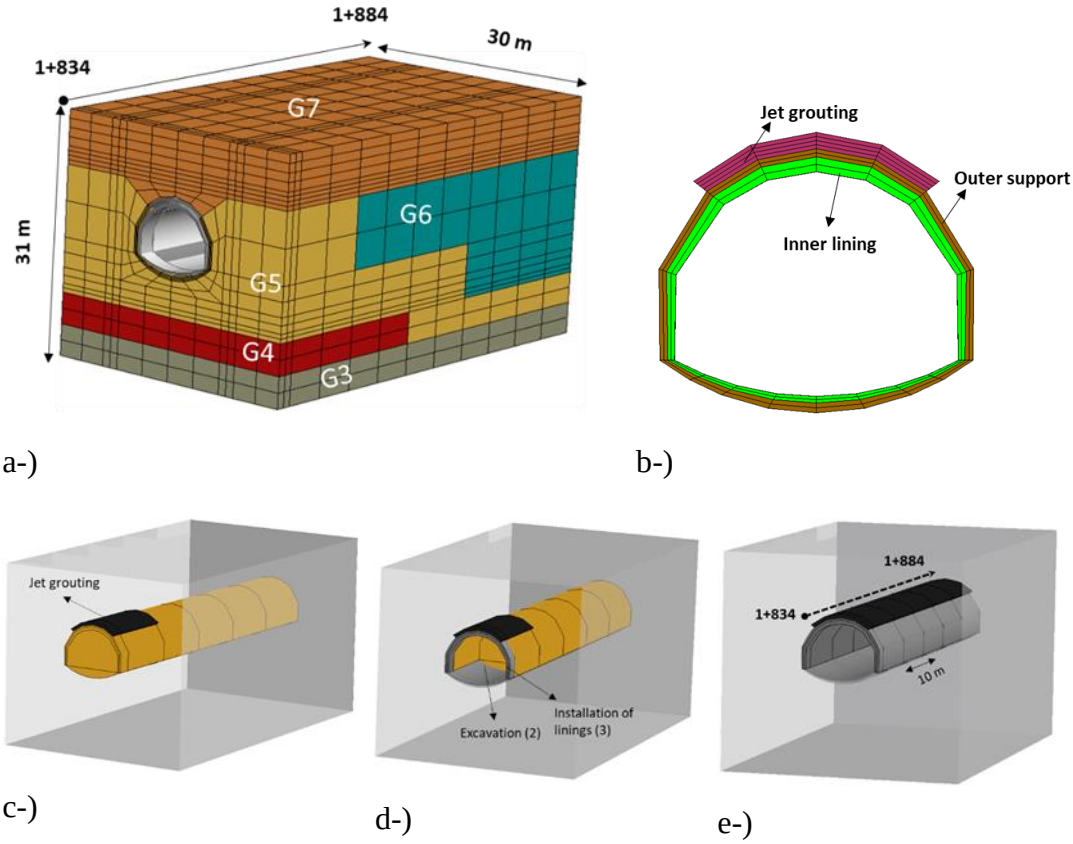


Figure 1. Model geometry and the distribution of granites (a). Detail of cross section showing the two support layers and the jet-grouting (b). Construction sequence: Construction of the first 10m long segment of the jet umbrella (c); excavation of tunnel (d); installation of support (e).

The 50-meter-long tunnel section was subdivided into five segments (**Figure 1e**), with individual lengths specified in **Table 1**. A 0.6-meter-thick jet grouting "vault" umbrella was constructed incrementally. **Figure 1c** illustrates the installation of the first segment of the jet grouting vault, a process assumed to be completed within 24 hours. The overall tunnel construction adhered to the timeline presented in **Table 1**, where the initiation dates for each jet grouting segment reflect the actual field construction sequence. The

numerical simulation covers a total duration of 114 days, beginning on January 27th, 2023, and encompasses the full execution of the 50-meter tunnel section.

Table 1. Timeline considered in the tunnel construction.

Step	Starting date	Location	Duration (days)	Interval
1	27.01.2023	1.834	14	0-14
2	10.02.2023	1.844	13	14-27
3	23.02.2023	1.854	20	27-47
4	13.03.2023	1.864	17	47-64
5	30.03.2023	1.874	21	64-85
6	20.04.2023	1.884	29	85-114

For the soils, an associated Mohr-Coulomb elasto-plastic constitutive model was adopted. The corresponding material parameters are presented in **Table 2** and were derived from values provided in the official project documentation.

Table 2. Material model parameters for the soils.

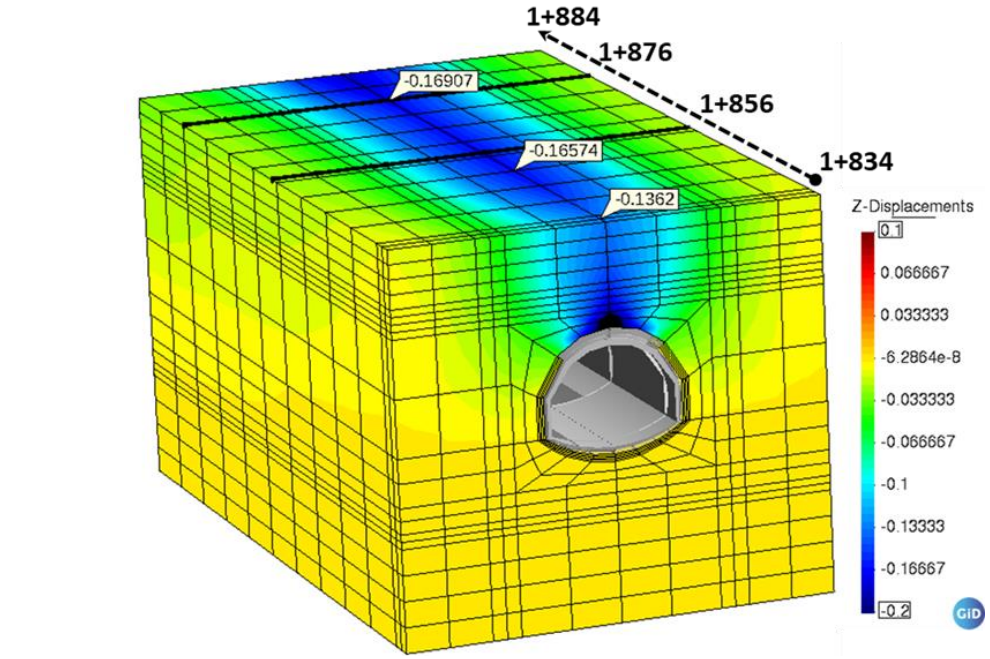
Soil	γ (kN/m^3)	E (MPa)	c' (kPa)	ϕ' (º)	K_0
G4	22	500	100	40	0.50
G5	20	120	25	35	0.40
G6	19	45*	5	32	0.35
G7	19	10	0	28	0.55

Simulating the installation of jet grouting columns, along with the formation of irregular cavities due to fluid spill-out, and the delayed deformation or collapse of these cavities, presents a highly complex modeling challenge. To address this, the adopted approach involved defining a continuous volume representing the entire set of jet grouting columns, modeled as a material capable of undergoing volumetric deformation governed by a viscous law.

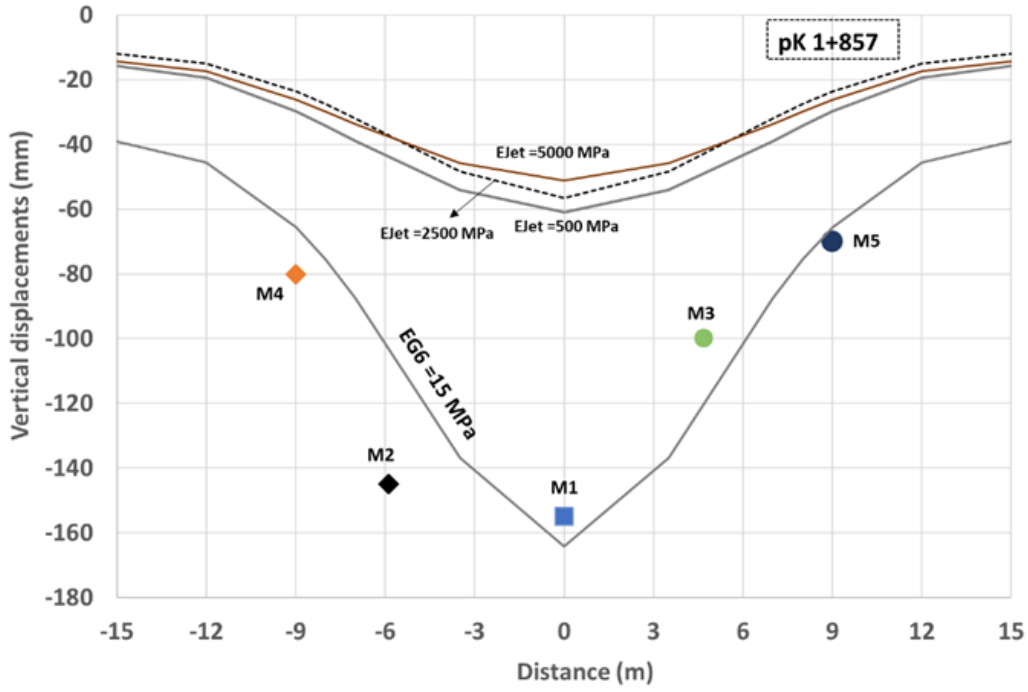
2. Modelling Results

Figure 2a presents the model geometry along with the locations of monitoring sections used to track surface settlements. For example, at station pK 1+876, settlements were recorded using monitoring plates M1, M2, and M3. The values on the figure correspond to the calculated vertical displacements (m) at the end of the 114-day construction period simulated.

Figure 2b presents a comparison between measured and simulated surface settlements. The agreement is reasonably good, with the model accurately capturing the final settlement magnitudes. The figure also includes a comparison scenario assuming properly executed jet grouting. Under such ideal conditions, the maximum predicted surface settlements range from 40 to 60 mm, depending on the elastic modulus of the jet-grouted material. In contrast, the actual field case experienced up to 160 mm of settlement, primarily due to volumetric strain induced by inadequate jet grouting execution. The model effectively captures this behavior by incorporating a viscous deformation mechanism, enabling the simulation of volume loss associated with poor grouting performance.



a-)



b-)

Figure 2. Distribution of vertical displacements at the end of simulation (a), comparison of final settlements at pK 1+857 in different model configurations (b).

3. Conclusions

This extended abstract presents simulation results, obtained using the CODE_BRIGHT [iii], to analyze the surface settlements observed during the construction of a reference urban tunnel. The observed settlements are attributed to a "volume loss" mechanism resulting from the defective jet grouting application. In the model, this volume loss is represented by characterizing the jet-grouting as a visco-plastic material capable of undergoing volumetric deformation over time. This approach allows for the simulation of the progressive settlement behavior induced by the defective grouting application, thereby capturing the essential aspects of the ground response under such compromised support conditions.

The simulation of measured surface settlements indicates that the observed deformations cannot be attributed solely to low-stiffness soil layers. Instead, the settlements are consistently explained by a loss of volume within the jet grouting umbrella, resulting from faulty construction of the jet grouting columns. This volume loss mechanism is essential to replicate the magnitude and distribution of the observed settlements. Additionally, the damage and voids generated during the construction of umbrella lead to generalized volume loss in the surrounding soil, extending well ahead of the tunnel face. This behavior is effectively captured by the model and is supported by the interpretation of the measured settlement data.

References

[i] Spira, Y., Lackner, R., & Pichler, C. (2005). Viscoplastic material models for soil: New insights into the soil-support interaction in NATM tunnel excavations. Archives of Mechanics, 57(6), 491-514.

[ii] Pichler, C., & Lackner, R. (2004). Optimization of jet-grouted support in NATM tunneling. Numerical and Analytical Methods in Geomechanics, 28(12), 1189-1210.

[iii] Olivella, S., J. Vaunat, and Rodriguez-Dono. A., Code_Bright 2023 user’s guide. 2023.

MODELING RAINFALL-INDUCED SLOPE FAILURE WITH CODE_BRIGHT

A. Rodriguez-Dono[*†], E. Badakshan[*], M. Buitrago[†], F. Song[§], Y. Wei[‡], S. Olivella[*†], J. Vaunat[*†], A. Priegue[†], S. Valero[†], O. Fruitos[†]

[*] Department of Civil and Environmental Engineering, Universitat Politècnica de Catalunya (UPC), 08034 Barcelona, Spain. First author's e-mail: alfonso.rodriguez@upc.edu

[†] International Centre for Numerical Methods in Engineering (CIMNE), 08034 Barcelona, Spain

[§] School of Aerospace Engineering and Applied Mechanics, Tongji University, Shanghai, China

[‡] School of Civil Engineering, Suzhou University of Science and Technology, Suzhou, China

Key words: Slope stability; Climate change; Coupled THM; Geomechanics; Resilience

Abstract. *This study investigates the effects of climate change on slope stability using CODE_BRIGHT, an advanced geotechnical simulation tool for coupled Thermo-Hydro-Mechanical-Chemical (THMC) processes. The Montjuïc slope in Barcelona serves as a case study for simulating rainfall infiltration, suction reduction, and progressive failure in unsaturated soils. The analysis incorporates advanced constitutive models (including Drucker-Prager, CAP, and Hyperbolic Mohr-Coulomb) and accounts for heterogeneity, anisotropy, and fracture-induced changes in permeability. Simulation results are integrated into the RESILMOB platform, which enhances real-time risk assessment through Hybrid Artificial Intelligence (HAI) trained on historical data and CODE_BRIGHT outputs. The combined framework enables early warning and decision support for resilient infrastructure design under evolving environmental conditions.*

1 INTRODUCTION

Landslides represent a critical geotechnical hazard, increasingly exacerbated by climate change, posing considerable risk to human life and property. Understanding how slopes respond to rainfall and what factors lead to their instability is a key focus in geotechnical engineering. Recent advances in multi-physics modeling have improved our ability to analyze the effects of climate and rainfall on slope stability, including the role of vegetation, meteorological variability, and soil heterogeneity[i,ii,iii,iv].

Climate change influences slopes through dynamic variations in moisture content, temperature gradients, and biochemical processes that alter soil properties over time[i,v]. Figure 1 illustrates projected changes in average annual temperature and precipitation in Europe, which are expected to impact slope stability by altering rainfall patterns and increasing the frequency of extreme events[v]. According to the European Environment Agency, temperatures will increase significantly in southern and eastern Europe, while precipitation will decrease in Mediterranean regions and increase in the north. The frequency and intensity of extreme events, such as heavy rains and droughts, will increase, affecting the stability of slopes[v].

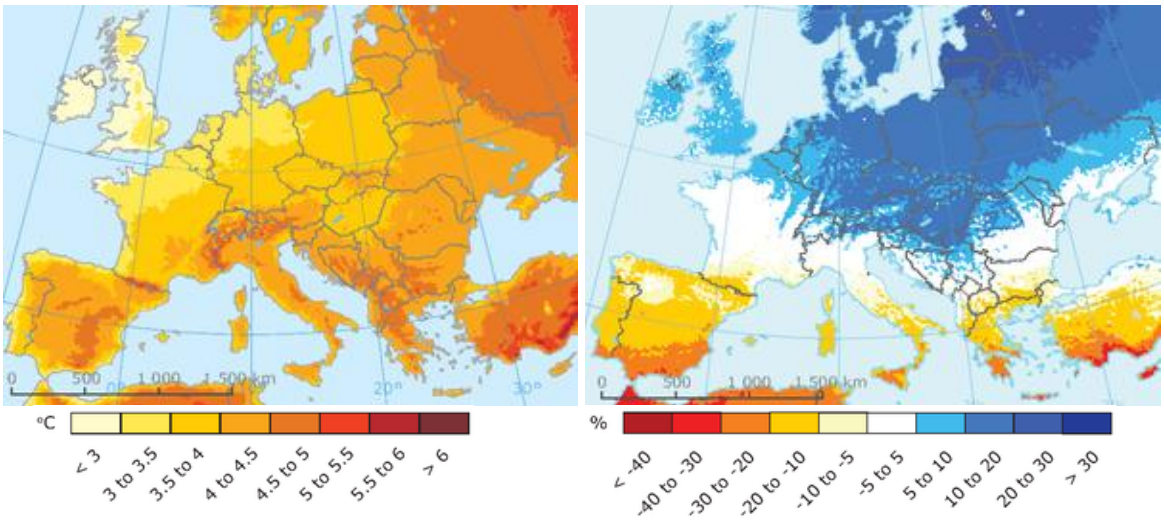


Figure 1: Projected changes in mean annual temperature (left) and annual precipitation (right) in Europe for 2071–2100 compared to 1971–2000[v]

Recent research using coupled numerical models has demonstrated the importance of simulating rainfall infiltration, suction changes, and the effects of soil heterogeneity and anisotropy on slope stability[ii,iii,iv,vi]. However, most traditional methods do not fully capture the complexity of these interactions or the progressive failure mechanisms triggered by climate extremes. There is a growing need to combine advanced numerical modeling with real-time monitoring and data-driven approaches for effective risk assessment and early warning in landslide-prone areas[ii].

2 RESILMOB PROJECT

The RESILMOB project addresses the effects of climate change on slope stability[i,ii,v], including increased global average temperature, intensified and more frequent extreme weather events, and significant changes in precipitation patterns. Both gradual (e.g., progressive loss of vegetation) and extreme events (e.g., heavy rains) directly impact slope stability, causing phenomena such as soil desiccation, erosion, collapses, and critical deformations due to rapid wetting and dynamic changes in pore pressure.

RESILMOB is a platform for monitoring and predicting the stability of geostructures using Hybrid Artificial Intelligence (HAI), advanced simulations, and in-situ data capture. Local simulations are connected to a common database containing geometric, geological, and climatological data obtained through aerial image processing and ground sensors, enabling detailed terrain representation and real-world validation[ii].

In the initial architecture, user interaction occurs at two levels: web and local. The SYNTHETIC DATA GENERATION/USE/PREDICTION module includes local pre- and post-processing interfaces for geostructural simulation programs, retrieving input from the DATA CAPTURE AND STORAGE module and geometric information from aerial images, geological, geotechnical, and climatological data. Model specifications are supplied by the user to the INTERFACE WITH THE USER web module, including UTM coordinates and boundary conditions of the geostructure.

3 CODE_BRIGHT FOR PARTIALLY SATURATED SOILS

CODE_BRIGHT is an advanced tool designed for the analysis and simulation of coupled THMC processes in geological media[vii,viii]. Its theoretical approach consists of an integrated system of governing equations, a set of constitutive laws, and a specialized computational approach that ensures accuracy and robustness in solving complex problems. The code is written in FORTRAN, using a modular architecture composed of multiple subroutines, which ensures flexibility and efficiency in its execution. CODE_BRIGHT integrates with the GiD system for pre- and post-processing[viii].

CODE_BRIGHT supports several constitutive models for simulating unsaturated soils; this study focuses on the Drucker-Prager, CAP, and Hyperbolic Mohr-Coulomb models. Within the RESILMOB project, these models are applied to the stability analysis of the Montjuïc slope to evaluate the impact of different suction and saturation scenarios, particularly those derived from periods of intense rainfall[ii]. The simulations show how these changes affect the mechanical properties of the soil, identifying critical displacements and plasticization zones that compromise its stability. Also, the simulations show how the resistance of the ground decreases progressively as the suction is reduced by the effect of water infiltration, explaining the progressive collapse of the soil in critical areas of the slope[ii].

The Drucker-Prager model is widely used in soil and rock mechanics to describe the plastic behavior of materials with internal cohesion and friction. It is an extension of the Mohr-Coulomb criterion to three-dimensional space, employing a smoothed yield surface that facilitates numerical implementation and convergence in complex simulations. More information about this model and its equations can be found in the CODE_BRIGHT User's Guide[viii]. The equation of the Drucker-Prager yield function F is expressed in Eq. 1, where q is the deviatoric stress, p' is the effective mean stress, δ is a model parameter, c is cohesion, and β is a strength parameter related to the internal friction angle. In CODE_BRIGHT, the Drucker-Prager model is used to analyze partially saturated soils and other geological materials subject to complex stress conditions, incorporating the influence of matrix suction, a key factor in unsaturated soils that affects apparent cohesion and shear strength[viii] (Figure 2). Apparent cohesion, as it depends on suction s (Eq. 2), varies significantly under changing climatic conditions. a_c and b_c are constants.

$$F=q-\delta p'-c\beta \tag{1}$$

$$c = a_c + b_c s \tag{2}$$

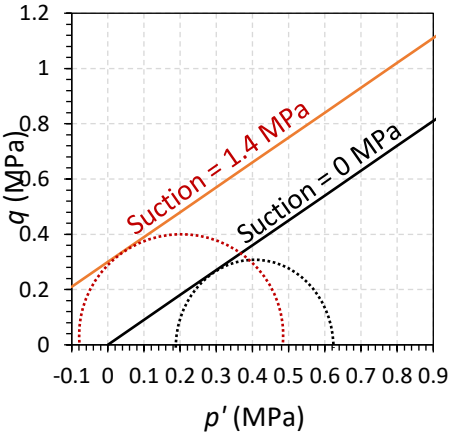


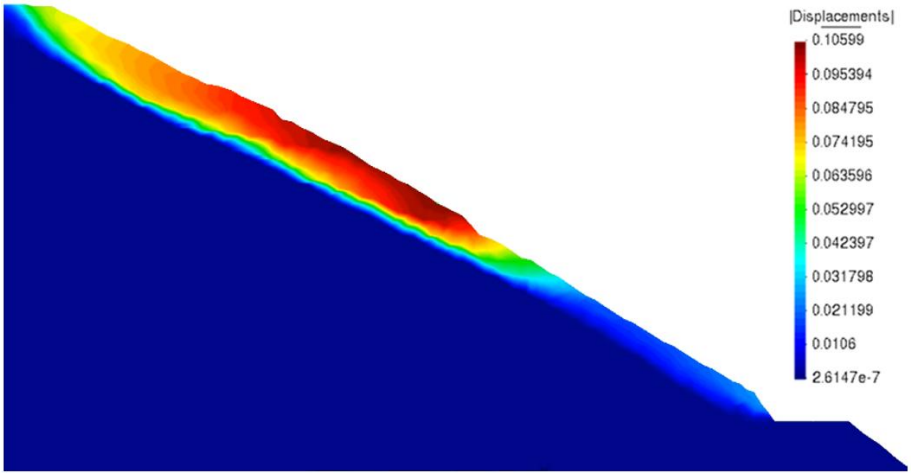
Figure 2: Drucker-Prager yield criterion and influence of suction on apparent cohesion.

4 RESULTS AND DISCUSSION

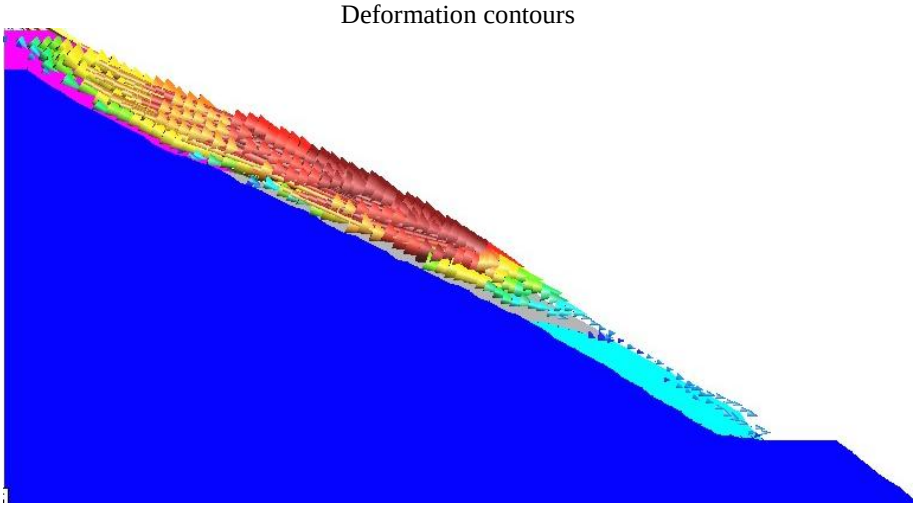
The application of CODE_BRIGHT to the Montjuïc slope demonstrates that rainfall infiltration leads to the reduction of suction and, consequently, a loss of soil cohesion and mechanical strength[ii,viii]. The simulations capture the development of critical displacements and plasticization zones, corresponding to observed failure mechanisms (Figure 3 and Figure 4). The integration of heterogeneous and anisotropic soil properties enhances model realism and predictive accuracy[iii,iv,vi].

The RESILMOB system's HAI component, trained on historical simulations and meteorological data, enables daily risk predictions and automated alerts. This hybrid approach supports continuous monitoring and real-time decision-making, enhancing operational safety for at-risk infrastructure.

Comparisons with documented slope failures validate the accuracy and efficiency of the simulations. The combined use of CODE_BRIGHT and HAI demonstrates a robust framework for early warning and proactive hazard management under changing climate scenarios.



Deformation contours



Displacements vectors

Figure 3: Final displacements in the slope (m) caused by rainy periods.

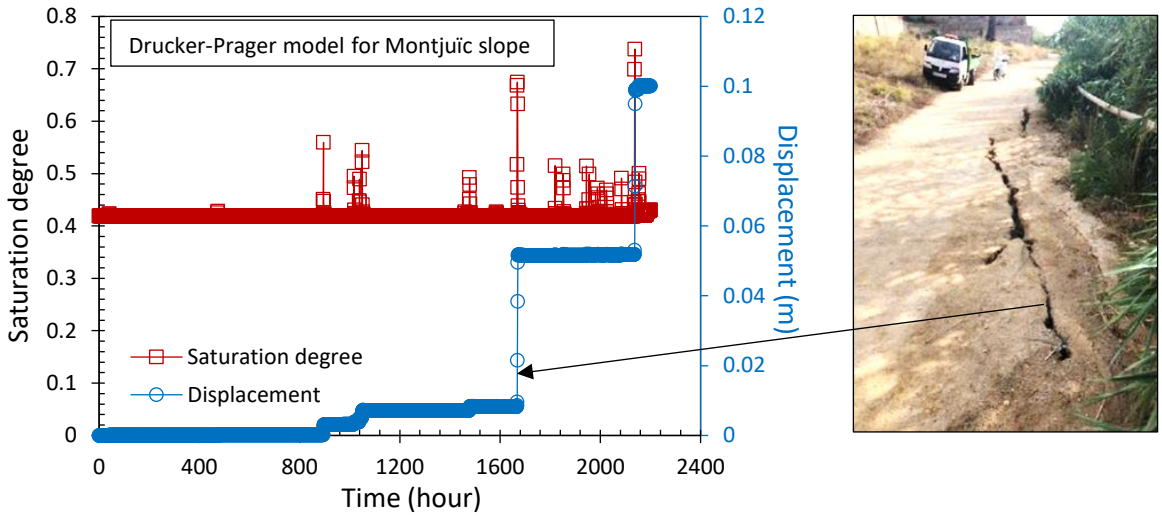


Figure 4: A time-series representation of displacement and liquid saturation degree evolution.

5 CONCLUSIONS

This research demonstrates the value of integrating advanced geotechnical simulation tools with hybrid AI for climate-resilient infrastructure. CODE_BRIGHT effectively models the complex interactions driving slope instability under variable climate conditions. The RESILMOB system operationalizes these insights, providing real-time risk assessment and early warning capabilities. These tools support the design and management of infrastructure in landslide-prone areas, contributing to greater resilience amid evolving environmental challenges.

REFERENCES

[i] Badakhshan, E., Vaunat, J., Veylon, G. (2024). Meteorological and vegetation effects on the thermal analysis of slopes. Renewable and Sustainable Energy Reviews, 196, 114352.

[ii] Duan, G., Song, F., Wang, H., Rodriguez-Dono, A., Wang, L., Chen, J. (2024). Stability analysis of unsaturated loess slopes subjected to extreme rainfall incorporating creep effects. Computers and Geotechnics, 169, 106231.

[iii] Rodriguez-Dono, A., Zhou, Y., Olivella, S. (2023). A new approach to model geomaterials with heterogeneous properties in thermo-hydro-mechanical coupled problems. Computers and Geotechnics, 159, 105400.

[iv] Rodriguez-Dono, A., Zhou, Y., Olivella, S., Gens, A. (2024). Modelling a gas injection experiment incorporating embedded fractures and heterogeneous material properties. Geomechanics for Energy and the Environment, 38, 100552.

[v] EEA (2015). Climate change impacts and adaptation. European Environment Agency. https://www.eea.europa.eu/soer/2015/europe/climate-change-impacts-and-adaptation.

[vi] Zhou, Y., Rodriguez-Dono, A., Olivella, S. (2024). A spatially correlated heterogeneous anisotropic model for simulation of gas flow in Callovo-Oxfordian claystone. Computers and Geotechnics, 173, 106570.

[vii] Olivella, S., Gens, A., Carrera, J., Alonso, E.E. (1996). Numerical formulation for a simulator CODE_BRIGHT for the coupled analysis of saline media. Engineering Computations, 13(7), 87-112.

[viii] Olivella, S., Vaunat, J., Rodriguez-Dono, A. (2024). CODE_BRIGHT User's Guide. Civil and Environmental Engineering Department. Universitat Politècnica de Catalunya – BarcelonaTech.

[ix] Sun, Y., Zhang, X., Li, W., Wang, G. (2021). Effects of rainfall intensity and duration on the failure mode and stability of unsaturated slopes. Landslides, 18, 1371–1384.

[x] Zeng, Q., Wang, G., Sassa, K. (2016). Influence of precipitation patterns on landslide activity: a case study from the Three Gorges Reservoir area, China. Natural Hazards, 82, 1209–1225.

COUPLED FLOW-DEFORMATION PROCESSES ASSOCIATED WITH THE REMOVAL OF ROOT WATER UPTAKE

Christopher Walker*, Ana Heitor*, Fleur Loveridge*, Jared West *, Jeff Gaucher† and Murphy Smith†

* School of Civil Engineering, University of Leeds, Woodhouse Lane, Leeds, LS2 9JT UK
E-mail: c.b.walker@leeds.ac.uk and a.heitor@leeds.ac.uk , web page: https://eps.leeds.ac.uk/civil-engineering

† William Hunt Consulting/Optera
48 Queens Road, Coventry, West Midlands.CV1 3EH, UK
Web page: https://optera.co.uk/

Key words: Root water uptake, HM coupled analysis, natural rehydration

Abstract. *The costs of repairs and rehabilitation of built infrastructure associated with shrink–swell processes in expansive soils are estimated to run into several billion pounds annually in the UK. This together with the seasonal moisture deficit caused by trees and vegetation root water uptake (intensified over the summer months), can cause subsidence due to ongoing clay shrinkage and consequently damage to infrastructure (e.g. residential and commercial buildings). This paper focusses on the modelling of coupled flow deformation processes associated with the removal of a mature tree in expansive soil. The Barcelona Expansive model (BExM) is implemented in a case study in London clay and the results indicate that the model can predict natural rehydration processes taking place upon the removal of mature trees.*

1 INTRODUCTION

The use of vegetation in infrastructure is relatively well established due to its low carbon and environmental footprint benefits. In fact, despite the different reinforcement mechanisms associated with vegetation being established for low plasticity soils, e.g. physical (root reinforcement [i]), chemical (nutrient uptake [ii]) and hydraulic (root water uptake [iii, iv]), there is a lack of understanding of the coupled processes and its impact in ground conditions composed of high plasticity soils, i.e. prone for shrink and swell. The prevalence of these ground conditions in the UK (Figure 1) is substantial and not surprisingly annually over 40,000 insurance claims valued at £400 million are made in relation to damage to residential and commercial buildings and buried infrastructure caused by vegetation induced shrinkage and subsidence ([v], [vi], [vii]). In addition, with climate change contributing to increasingly hotter summers [viii] the moisture deficit caused by root water uptake particularly for high water demand species exacerbates the soil deformation, i.e. shrinkage. The current mitigation strategy typically includes vegetation and/or tree removal. However, the timescales associated with natural ground rehydration and associated volume change are often not known. This poses substantial challenges with the scheduling of the infrastructure's rehabilitation works.

In this paper, a case study examining the timescale for natural rehydration is outlined. Code_Bright (CB) [ix] is used to model natural rehydration using the Barcelona Expansive Model (BExM) and parameters for London clay to mimic a typical site in the south of England.



Figure 1: Shrink–swell clay potential in the UK (content from British Geological Survey materials © UKRI [2021] reproduced under the Open Government Licence https://www.nationalarchives.gov.uk/doc/open-government-licence/version/3/ [x])

2 CASE STUDY SITE AND TREE SPECIES

A typical site composed of London clay inspired by a case study reported by Biddle [vi] (Figure 2) is examined in this paper. The site is located Barham Park, Wembley and was selected for its uniform ground conditions and seemingly little interference from other vegetation producing a simple moisture distribution. The ground is composed mainly of London clay with a liquid limit of 84% and plasticity index 57% measured at 2.4m from the tree (Figure 2). The moisture deficit was driven by a Horse Chestnut tree with a height of 14m and trunk diameter of 0.71m measured in 1994 and 1992, respectively. The site investigation campaign performed by Biddle [vi] involved time lapsed monitoring of changes in volumetric water content in the ground using a neutron probe up to 3.7m below ground level in permanent access tubes. For this paper the soil moisture distribution measured on the 29/10/1991 was selected for modelling which shows a significant reduction in moisture from the spring average values. Figure 2 shows the comparison between moisture content distribution on the 29/10/1991 and spring average for both 2.4m and 4.8m away from the tree. This data was used to define initial moisture and suction conditions in the ground, as detailed information about the tree physiology was not available. The ground water level was inferred to be at 4 below ground level. More details are available in Biddle [vi].

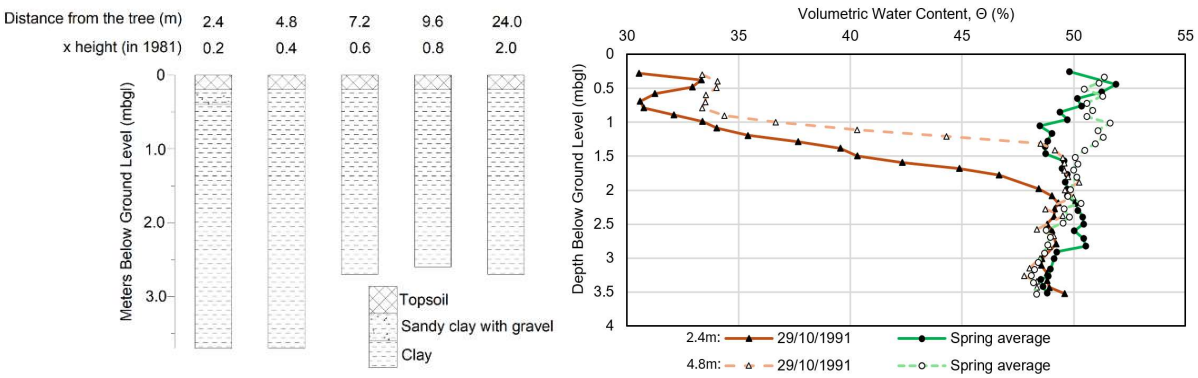


Figure 2: Ground investigation (left) comparison between moisture content distribution on the 29/10/1991 and spring average for both 2.4m and 4.8m from the tree (right) (modified after Biddle [vi]).

3 FINITE ELEMENT MODEL IN CODE BRIGHT

A 2D axisymmetric model with rotational symmetry around the trunk of the tree was selected. To minimise boundary effects the model domain selected was 11.5m in depth and 25m in length. A hydro-mechanical solution was considered, and any thermal effects ignored. An unstructured mesh was adopted with finer local mesh sizes applied to the boundaries in proximity to the tree. For modelling the soil behaviour the BExM was selected and the calibration of parameters for London clay are presented in the subsequent sections.

3.1 Water retention properties calibration

The soil water retention curve (SWRC) and water retention parameters[xi] (Eq. 1) were estimated from results for London clay[xii]. The hydraulic conductivity curve (Eq. 2) was then determined using Mualem [xiii] model. The parameters adopted are shown in Table 1.

$$S_e = \frac{S_l - S_{rl}}{S_{ls} - S_{rl}} = \left(1 + \left(\frac{P_g - P_l}{P}\right)^{\frac{1}{1-\lambda}}\right)^{-\lambda} \quad (1)$$

$$k_{rl} = \sqrt{S_e}\left(1 - \left(1 - S_e^{1/\lambda}\right)^{\lambda}\right)^2 \quad (2)$$

Symbol (see Eq 1 and Eq 2)	Value	Symbol (see Eq 1 and Eq 2)	Value
P	0.125	Sr(res)	0.1
m	0.15	Sr(sat)	1
n	1.18	m	0.15
		Ksat (m/s)	5.0×10^{-9}

Table 1: London clay parameters adopted (nomenclature in line with Code_Bright [xiv]).

3.3 Mechanical behaviour calibration

As there was limited data available for quantifying the geomechanical behaviour of the case study site in the London clay, results reported in previous studies were used instead. The one-dimensional consolidation data for tests conducted at constant suction by Monroy et al[xv] were used for calibrating BExM mechanical parameters. The tests comprised of saturation of compacted London clay at constant vertical stress and loading and unloading at constant suction. The London clay used in the tests had a liquid limit of 83%, plasticity index of 54% (relatively similar to case study site). The tests were simulated in CODE_BRIGHT in a simple 2D oedometer model. Parameters for macro and micro void ratio (e_{macro} & e_{micro}) and saturated preconsolidated stress (p_0^*) were taken from Monroy et al[xv]. The coupling parameters were taken from Toprak et al[xvi] for MX-80 bentonite and all other parameters derived from typical ranges presented literature and selected to ensure agreement with observed behaviour (Table 2). Figure 3 shows the comparison between the experimental data and CODE_BRIGHT (CB) prediction for different suction levels. It can be observed there was a relatively good agreement between the experimental results and predictions.

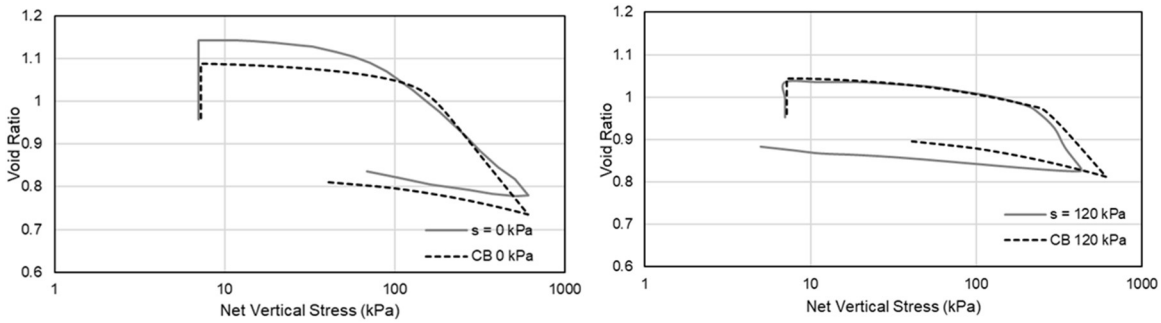


Figure 3: Mechanical behaviour calibration using experimental data from Monroy et al (2010)

Parameter	Unit	Value	Parameter	Unit	Value
Void ratio	-	0.95	f_{SI0}	-	-0.1
e_{macro}	-	0.59	f_{SI1}	-	2.2
e_{micro}	-	0.37	n_{SI}	-	0.5
κ^{macro}	-	0.04	M	-	1
κ^{micro}	-	0.001	r	-	0.7
κ_s^{macro}	-	0.06	β	MPa^{-1}	2
υ^m	-	0.3	p_c	MPa	0.001
K_{min}^{macro}	MPa	2	p_{c0}	MPa	0.1
K_{min}^{micro}	MPa	0.001	κ_s	-	0.8
f_{SD0}	-	-0.1	$\lambda(0)$	-	0.15
f_{SD1}	-	1.1	p_0^*	MPa	0.1
n_{SD}	-	2			

Table 2: BExM London clay parameters (nomeclature in line with Code_Bright[xiv])

3.4 Initial ground conditions with moisture deficit

The case study site provided good quality data of moisture distribution in the ground induced by tree root water uptake. Based on the information available the following assumptions were made:

a) the moisture deficit from the tree was assumed to extend to 1.5m deep and 6.5 laterally.
b) Below 1.5m ground level, field conditions are established
c) The suction levels in the root zone follow a relatively linear distribution up to 1.5m deep

The profile of moisture was simulated in the CODE_BRIGHT model by splitting the area of moisture deficit (6.5m by 1.5m) into three 0.5m thick horizontal layers allowing for the application of prescribed liquid pressures, linearly reducing with depth, at each boundary to match the measured moisture distribution. The maximum liquid pressure applied at the surface of the moisture deficit area was approximately 1 MPa and was initially selected as it was within the wilting point threshold for common tree species in the UK. Figure 4 shows there is good agreement with the soil moisture deficit (SMD) from the CODE_BRIGHT model utilising the selected water retention and BExM parameters and the Biddle [vi] field results.

To simulate the natural hydration process in the ground after tree removal, the boundary conditions set to generate realistic values for soil moisture deficit distribution in the model are removed. This allows the original field capacity conditions controlled by the position of the ground water level to be reestablished. A relatively long-time step of 4 years is considered in the analysis to ensure equilibrium conditions are achieved and natural rehydration completed.

3 RESULTS AND DISCUSSION

Figure 5 shows the saturation contours obtained during the natural rehydration process up to 3years. Not surprisingly, in the 1st year there is a small change in the degree of saturation around the root zone. In contrast, after 2 years there is a substantial increase in the degree of saturation (e.g. change from 0.75 to 0.9 in the root zone). This simulates well what happens in the field and agrees with anecdotal evidence provided by Biddle [vi] and residential infrastructure insurance providers. It should be noted that it is only after 3 years field conditions are re-established. Figure 6 shows that the surface deformation patterns follow similar timescales, with larger displacements in the first 2 years. Similarly, there is a substantial reduction in the change of displacement observed after 3 years. Having a good understanding of these timescales is critical to inform timing for maintenance operations to avoid further damage to infrastructure.

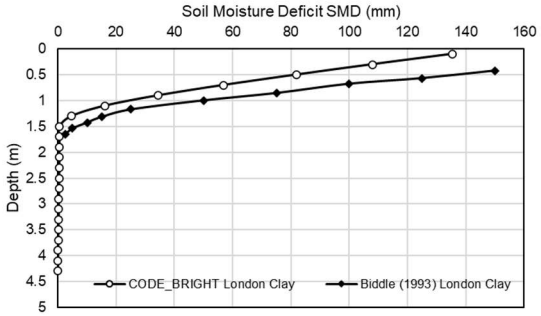


Figure 4: Comparison between measured and assumed moisture deficit at 2.4m away from the tree taken on the 29/10/1991 (units refer to mm of water column pressure).

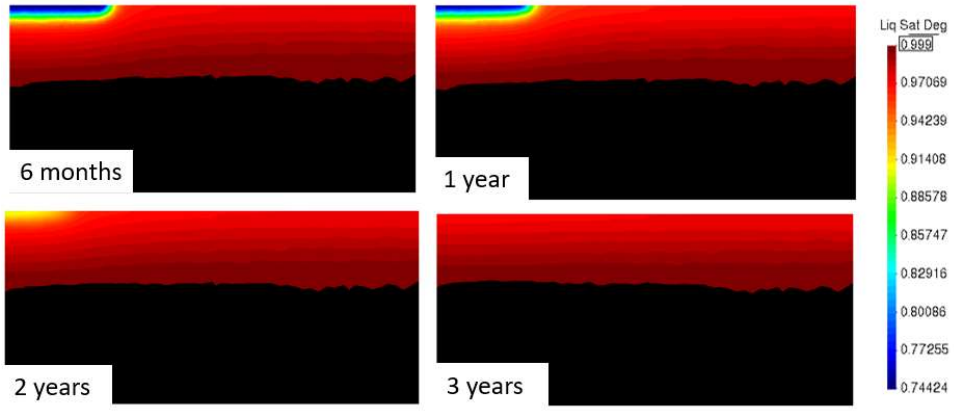


Figure 5: Variation of the degree of saturation after removal of the tree caused by natural rehydration.

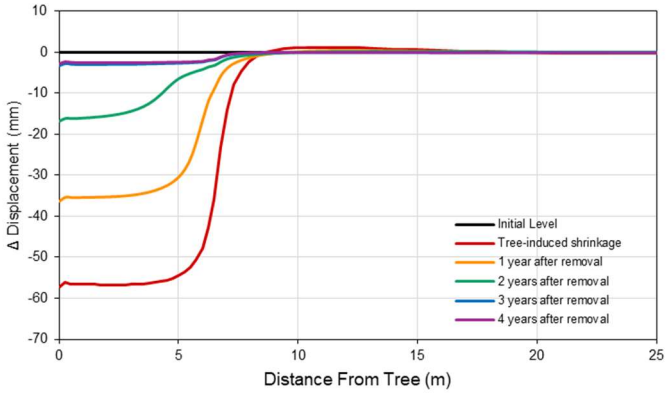


Figure 6: Change in vertical displacement from tree measured at ground level

11 CONCLUSIONS

The results of the CODE_BRIGHT model developed with the support of field data were capable of matching field moisture deficit conditions of the case study site. Additional data from the previous studies for London clay was used to evaluate best fit parameters and a natural rehydration process was successfully modelled. While the results were not quantitively evaluated, they are generally in agreement with timescales supported by anecdotal observations by the authors. A more detailed field campaign is currently being planned to gain further understanding of coupled flow-deformation process associated with natural rehydration. While these results are still preliminary, they can be used to inform the development of better asset management practices for locations where damage to residential and urban infrastructure caused by root water uptake is significant.

ACKNOWLEDMENTS

Funding from UKRI via Impact Acceleration Account and Optera is gratefully acknowledged.

REFERENCES

[i] Galpathage, S. G., Indraratna, B., Heitor, A. and Rujikiatkamjorn, C. (2019) ICE J. of Ground Improvement, https://doi.org/10.1680/jgrim.18.00105

[ii] Pathirage, U., Indraratna, B., Pallewattha, M., Heitor, A. (2017) ICE J. of Environmental Geotechnics, http://dx.doi.org/10.1680/jenge.15.00065

[iii] Pallewattha, M., Indraratna, B., Heitor, A. and Rujikiatkamjorn C. (2019) Transportation Geotechnics, https://doi.org/10.1016/j.trgeo.2018.11.005.

[iv] Rouainia, M., Helm, P., Davies, O. et al. Acta Geotech. 15, 2997–3016 (2020). https://doi.org/10.1007/s11440-020-00965-1

[v] Mahon, D. (2024) Tree Related Subsidence Damage [Online] Available at: https://www.localsurveyorsdirect.co.uk/tree-related-subsidence-damage#:~:text=The%20average%20annual%20cost%20of,approximately%2040%2C000%20claims%20per%20year [Accessed 19/11/2023]

[vi] Biddle P.G Tree Root Damage to Buildings (Willowmead Publishing 1998, Oxford ISBN 095330860X)

[vii] Hekmati, N., Rahman, M.M., Gorjian, N. et al. SN Appl. Sci. 2, 1806 (2020). https://doi.org/10.1007/s42452-020-03581-6

[viii] Lowe, J.; Bernie, D.; Bett, P.; Bricheno, L.; Brown, S.; Calvert, D.; Clark, R.; Eagle, K.; Edwards, T.; Fosser, G.; et al. UKCP 18 Science Overview Report November 2018 (Updated March 2019). Availabe online https://www.metoffice. gov.uk/pub/data/weather/uk/ukcp18/science-reports/UKCP18-Overview-report.pdf [accessed on 11/05/2021]

[ix] CODE_BRIGHT is a Finite Element Method (FEM) program capable of performing coupled thermo-hydro-mechanical (THM) analysis in geological media. [Online] Available at: https://deca.upc.edu/en/projects/code_bright [Accessed on 22/05/2024]

[x] British geological survey (2012) GeoSure [Online] Available at: http://www.bgs.ac.uk/products/geosure/shrink_swell.html [Accessed 19/11/2023]

[xi] van Genuchten, M. Th. (1980). Soil. Sci. Soc. Am. J. 44:892-898.

[xii] Croney, D. (1977). The design and performance of road pavements. London: Her Majesty's Stationery Office.

[xiii] Mualem, Y. (1976). A new model for predicting the hydraulic conductivity of unsaturated porous media. Water Resour. Res. 12:513–522. doi:10.1029/WR012i003p00513

[xiv] Code_Bright Users's manual (2025). [online] Available at https://deca.upc.edu/en/projects/code_bright/downloads/users_guide/view [Accessed 15/02/2025]

[xv] Monroy, R., Zravkovic, L., Ridley, A. (2010). Geotechnique 60, No. 2, 105–119, doi: 10.1680/geot.8.P.125

[xvi] E. Toprak, E., Olivella S., Pintado X. (2020). Environ Geotech, 7 (1) pp. 72-94, 10.1680/jenge.17.00086

ANALYSIS OF THE STRESS MEASUREMENTS IN "IN SITU" TESTS. EXAMPLE OF THE FULL-SCALE TEST (FISST) IN FINLAND

Pintado, X.[*], Leino, T. [*], and Niskanen, M.[†]

[*] Mitta Engineering Oy
Riihimiehentie 3, 01720 Vantaa, Finland
E-mail: xavier.pintado@mitta.fi, teemu.leino@mitta.fi, web page: https://mitta.fi/en/
[†] Posiva Oy
Satamatie 22, 27160 Eurajoki
E-mail: mika.niskanen@posiva.fi, web page: http://www.posiva.fi

Key words: GiD interface, stress tensor, "in situ" test

Abstract. *The analysis of "in situ" tests is necessary for assessing the behaviour of the spent nuclear fuel repositories at short term and for validation and parametrization of constitutive models that will be used for carrying out simulations in long term. These simulations are necessary for safety case. One of the "in situ" tests measurements are the stresses. These measurements are performed with total pressure sensors, where only the position and orientation of the sensor, and the value of the stress, are given. The stress tensor needs six variables to be defined, and the orientation of the sensor probably will not follow any axis of the reference geometry. It will be necessary to transform the stress tensor at the reference geometry to the local axes defined by the position and orientation of the sensor. The sensors might be emplaced at the intersection between materials (e.g. rock and buffer) and some considerations concerning the differences between the stress state of both materials should be taken into account.*

1 INTRODUCTION

This contribution presents the analysis of the stresses calculated and measured during the the Full-Scale In-Situ System Test (FISST) currently ongoing in the ONKALO® demonstration area[i], part of the Finnish spent nuclear fuel disposal facility under commissioning phase. The demonstration tunnel hosting FISST is located at a depth of approximately 420 m. More details concerning this test can also be found in [ii] and [iii].

The test is instrumented with different types of sensors. Sensors measuring temperature (thermocouples), relative humidity (capacitive hygrometers and psychrometers), pore pressure (piezometers), total pressure (total pressure sensors) and electric resistance tomography (ERT) system were chosen based on the evaluation of suitable sensors and instrumentation methods done in the EU project Modern 2020 and from experiences in Prototype Repository[iv] and other "in situ" experiments. Part of the sensor data is used for comparing with the early evolution simulation results of the EBS system.

Effective stress evolution should be assessed for knowing the evolution of the swelling pressure. To do that, pore pressure and total pressure sensors were installed at different positions in contacts between buffer and rock and backfill and rock. Measuring both pressures, it is possible to assess the evolution of the swelling pressure once the buffer is fully saturated. In between (before the pore pressure sensors start to measure), total pressure sensors provide directly the swelling pressure. There are other sensors embedded in backfill but will not be discussed in this contribution.

2 TEST GEOMETRY

ONKALO® management sent the construction drawings, so it was possible to create the Digital Twin which represents the real geometry of the test (Figure 1, left). This geometry was used for carrying out the thermo-hydraulic (TH) analysis, performed with a finite elements mesh constructed with linear tetrahedrons. The thermo-hydro-mechanical (THM) analysis was carried out in a simplified geometry (Figure 1, right). In this case, the finite element mesh was constructed with linear quadrilateral prism elements with numerical integration (selective) with 8 points.

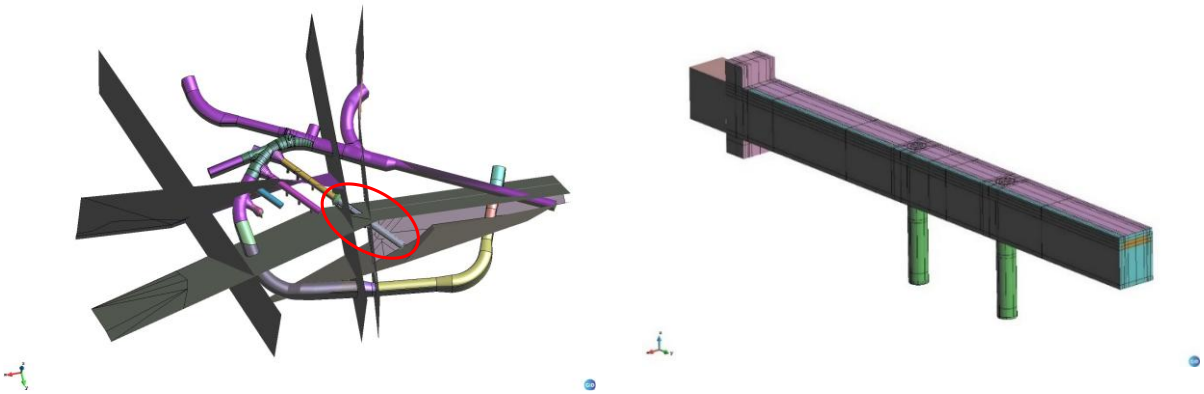


Figure 1: FISST emplacement with the network fractures' system for carrying out the TH analysis (left) and simplified geometry for carrying out the THM analysis (right).

Linear tetrahedrons should not be used in mechanical problems due to the risk of locking. GiD^{v} only can generate structured meshes in 3-D with quadrilateral prisms, so the geometry was simplified although the deposition holes kept the real geometry.

3 SENSORS DESCRIPTION

The position of the total (TP) and pore (PP) pressure sensors (at the same position in deposition holes) are presented in Figure 2 left (buffer) and Figure 3 right (backfill). The position of the sensors are nodes of the mesh (GiD allows this possibility).

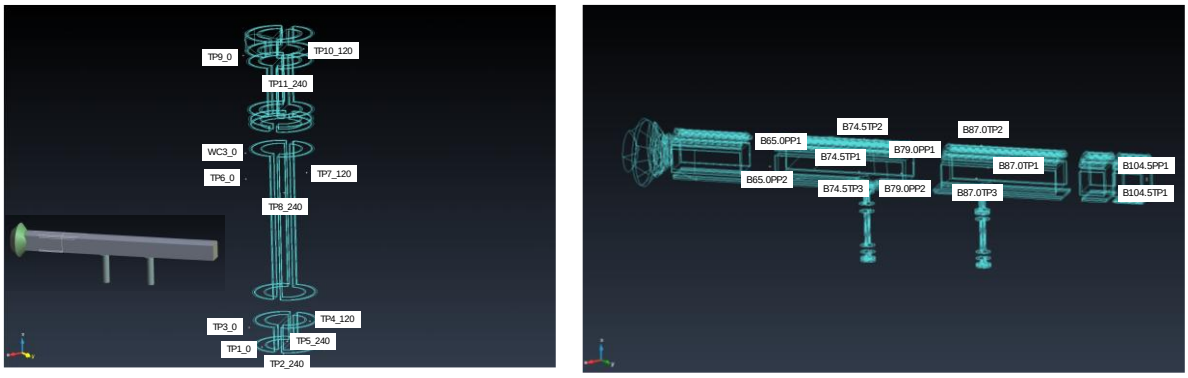


Figure 2: Total pressure sensors position in buffer. Pore pressure sensors with codes 15PP1_0, 15PP2_240, 15PP3_120, 15PP4_0 and 15PP5_240 are at the same position the sensors 15TP3_0, 15TP5_240, 15TP7_120, 15TP9_0 and 15TP11_240 respectively (left). Position of the total pressure (TP) and pore pressure (PP) sensors in backfill (right).

Total pressure sensors are vibrating wire Geokon 4800 and pore pressure sensors are vibrating wire Geokon 4500. Sensors are emplaced on the tunnel rock wall (Figure 3). In deposition holes, the sensors were emplaced together on a metal sheet fixed on the deposition hole walls. Measuring stresses in "in situ" tests is difficult[vi,vii].

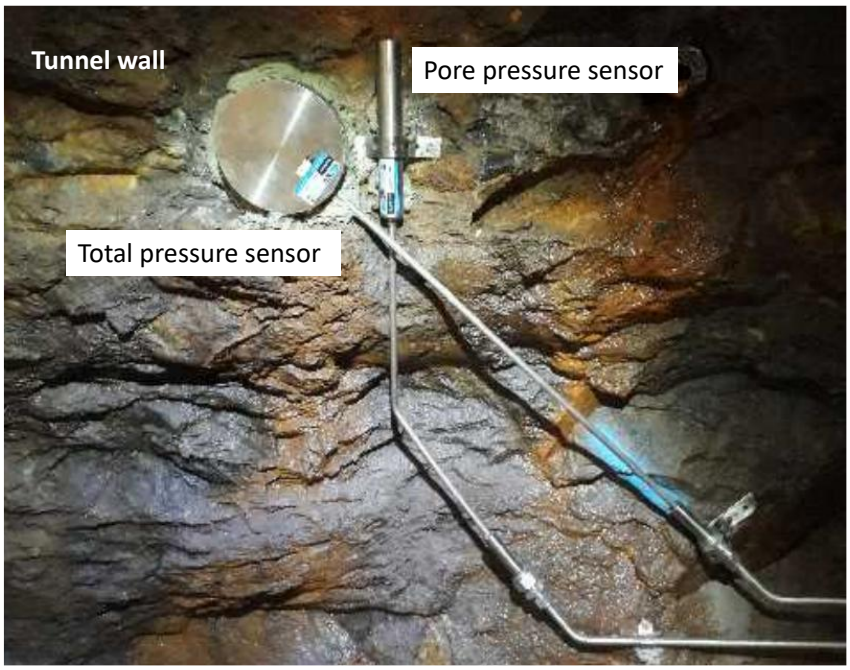


Figure 3: Total pressure and pore pressure sensors emplaced on the tunnel wall.

4 CALCULATION OF THE SENSOR STRESS (TOTAL PRESSURE)

The stresses are calculated at the Gauss points, but the sensors are located at the nodes. It is not possible to have the Gauss points on the rock walls unless the integration points are on the edges or faces of the element. This is not the case in the quadrilateral prisms available in CODE_BRIGHT[viii], so it is necessary to calculate the average of the stresses calculated at the Gauss points of the elements that have one node at the position of the total pressure sensor. To do that, it is necessary to work with three files:

- Sensors_Position (TXT file). Text file where there are the codification of the sensor and its coordinates, which are the coordinates of a node. This file should be prepared aside from the CODE_BRIGHT calculations' files.
- Root_gri (DAT file), where it is possible to identify the coordinates with the number of node where the sensor is located and the elements that have this node. It is also possible to identify the number of the element with the material. This will be important to distinguish buffer and rock elements.
- Root_Stress.post (RES file). This file contains the number of node and the stresses calculated at the Gauss points. The postprocessor can write the average of the stresses calculated at all Gauss points or the values in each Gauss point. Ideally, the average should be calculated with a weighted average considering the Gauss points closest to the node where the sensor is located. In this contribution, only the stress average was considered.

The rock and the buffer have different initial stresses when the bentonite starts to swell. For this reason and although the stresses are continuous in the axes orthogonal to the wall surfaces (equilibrium), the elements might be too large and this continuity cannot be achieved, so the stress orthogonal to the wall surface in the rock element and in the adjacent buffer element might be different. Due to the buffer element has the initial stress almost null, it is expected that its value will be more realistic than the stress calculated at the adjacent rock element, which will have the influence of the stresses before buffer emplacement.

The stress tensor has six components in 3-D using an arbitrary axes reference, and the normal vector of the sensor (orthogonal to the rock wall in this case) does not coincide with the chosen axes in general, so it is necessary to rotate the stress tensor in order to fit one of the new axes with the sensor normal vector. The z axis was chosen, so after two rotations, the new z'' axis fits with this vector. The rotations were (Figure 4):

- First rotation: α around z. α>0 if directed from x to y. α is the orientation of a dip with respect to y.
- Secondary rotation: β around y'. β>0 if directed from z' to x'. β is the inclination of a dip with respect to the horizontal plane.

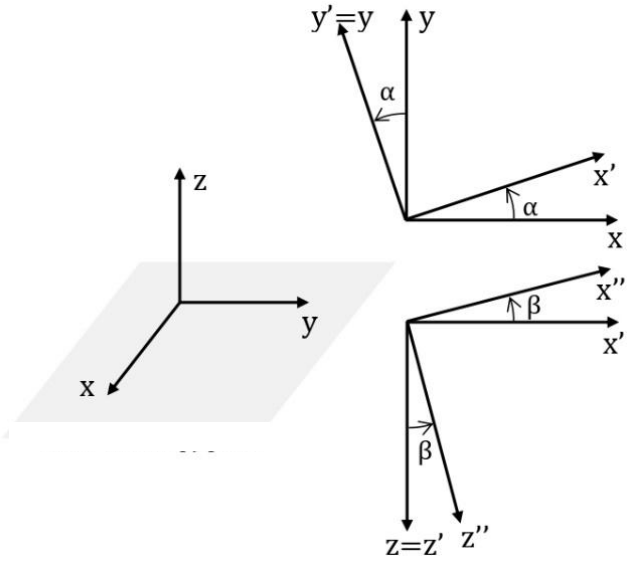


Figure 4: Position Convention of reference axes for transverse isotropic material [vi].

The double rotation of the stress tensor can be expressed as:

$$\begin{bmatrix} \sigma''_{xx} & \tau''_{xy} & \tau''_{xz} \\ \tau''_{xy} & \sigma''_{yy} & \tau''_{yz} \\ \tau''_{xz} & \tau''_{yz} & \sigma''_{zz} \end{bmatrix} = \begin{bmatrix} cos\beta \cdot cos\alpha & -cos\beta \cdot sin\alpha & sin\beta \\ sin\beta & cos\alpha & 0 \\ -sin\beta \cdot cos\alpha & sin\alpha \cdot sin\beta & cos\beta \end{bmatrix} \begin{bmatrix} \sigma_{xx} & \tau_{xy} & \tau_{xz} \\ \tau_{xy} & \sigma_{yy} & \tau_{yz} \\ \tau_{xz} & \tau_{yz} & \sigma_{zz} \end{bmatrix} \begin{bmatrix} cos\beta \cdot cos\alpha & sin\beta & -sin\beta \cdot cos\alpha \\ -cos\beta \cdot sin\alpha & cos\alpha & sin\alpha \cdot sin\beta \\ sin\beta & 0 & cos\beta \end{bmatrix}$$

Finally, $-\sigma''_{zz}$ is the measurement of the total pressure sensor. The negative sign is due to the compression pressure measured by the sensors was positive and CODE_BRIGHT considers the compression negative.

The process of reading the three files described above and the rotation is performed with a Python script. The results are prepared in an Excel file matrix where the first column presents the time and the corresponding stress (total pressure) of each sensor at the following columns.

Figure 5 presents the flow diagram for getting the stress state at the sensor's position before doing the rotation.

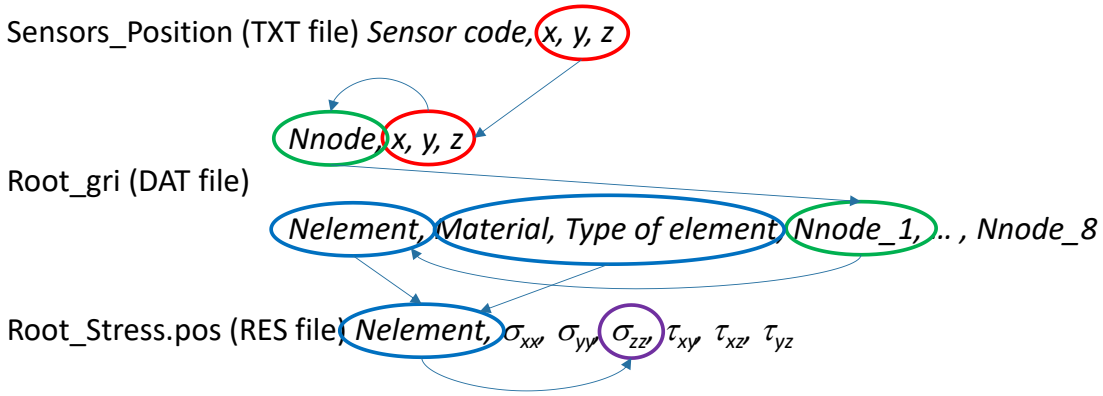


Figure 5: Flow diagram for getting the sensor stress before doing the rotation.

5 RESULTS

Figure 5 presents the total pressure evolution at the deposition hole closest to the plug (EH15) and at the backfill.

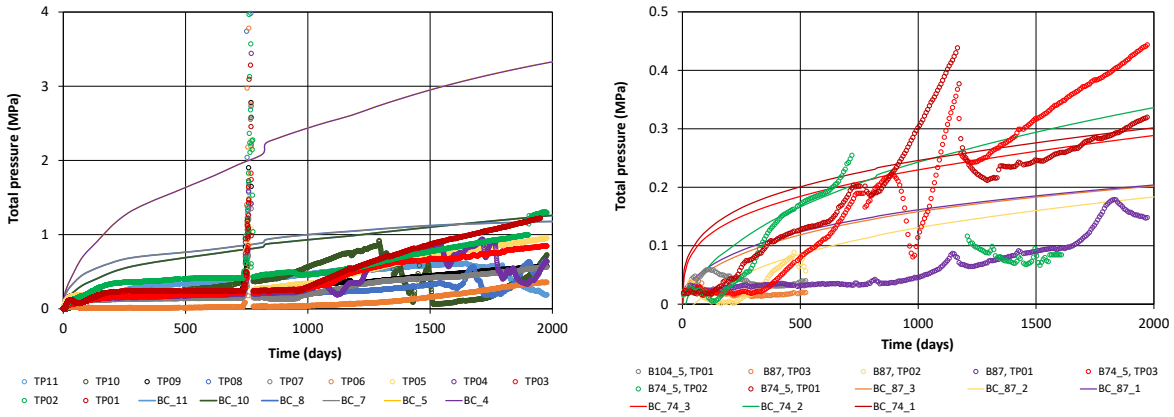


Figure 5: Total pressure evolution in EH15 deposition hole (the closest to the plug, left) and in backfill (right). The points are measurements and the solid lines calculations.

4 CONCLUSIONS

- The stresses are tensorial magnitudes with six components. The information provided by the total pressure sensors is just the stress in one direction.
- The stresses are calculated at the Gauss points, not at the nodes, so it is necessary to interpolate the calculations in the Gauss points for obtaining the stresses at the node where the sensor is located.
- It is necessary to rotate the stress tensor calculated for fitting one of the new local axes with the vector orthogonal to the sensor.
- The stresses are difficult to fit due to the complexity of the mechanical behaviour of bentontes and due to the difficulties measuring the stresses.

ACKNOWLEDGEMENTS

This work has been co-funded by the European Union under the Grant Agreement n°101166718) and Posiva Oy as part of the work ongoing into the EURAD-2 Work Package HERMES.

REFERENCES

[i] Posiva. Final disposal tests. Posiva website. https://www.posiva.fi/en/index/finaldisposal/finaldisposaltestsfisstytk.html (Retrieved April 22, 2025).

[ii] Tsitsopoulos, V., Holton, D., Appleyard, P., Thompson, S., Baxter, S., Niskanen, M. 2023. Thermal hydraulic and mechanical modelling of the full-scale in situ test (FISST). Engineering Geology 322: 107165.

[iii] Toprak, E., Olivella, S., Pintado, X., Kumpulainen, S., Hassan, M., Kristensson, O., Niskanen, M., 3D THM modelling of Full-Scale In-Situ System Test (FISST). Submitted to Geological Society, London, Special Publications.

[iv] Svemar, C., Johanesson, L-E, Grahm, P., Svensson, D., Kristensson, O., Lönnqvist, M., Nilsson, U. 2016. Prototype Repository Opening and retrieval of outer section of Prototype Repository at Äspö Hard Rock Laboratory. Summary report. SKB report TR 13-22. Stockholm, Sweden.

[v] CIMNE. GiD SMULATION. https://www.gidsimulation.com/ (Retrieved April 22, 2025).

[vi] Aitemin, NDA, Andra, NRG, Nagra, Enresa, Euridice, ETH Zurich, NRG, RWMC, DBE, TEC, Posiva, SKB, RAWRA, GSL. 2013. WP2 State of Art Report on Monitoring Technology. Modern EU project deliverable (D-N°: 2.2.2). Contract 232598.

[vii] García-Siñeriz, J. 2023. Instrumentation and Control System for Nuclear Power Plants. Chapter 13-Instrumentation for nuclear waste repository monitoring. Editor(s): Mauro Cappelli. Woodhead Publishing Series in Energy. Woodhead Publishing: 711-853. ISBN 9780081028360,

[viii] Olivella, S., Vaunat, J., Rodríguez-Dono, A. 2024. CODE_BRIGHT 2024 User's guide. Department of Civil and Environmental Engineering. Technical University of Catalonia. Barcelona, Spain, https://deca.upc.edu/en/projects/code_bright (Retrieved April 22, 2025)

SIMULATION OF THM PROCESSES FOR A GENERIC HLW REPOSITORY

Matthias Hinze[*] and Larissa Friedenberg[*]

[*] Gesellschaft für Anlagen- und Reaktorsicherheit (GRS) gGmbH
Repository Research Department
Theodor-Heuss-Straße 4, 38122 Braunschweig, Germany
E-mail: matthias.hinze@grs.de, web page: https://www.grs.de/en/

Key words: THM coupled analysis, CODE_BRIGHT, Geological media, HLW repository

Abstract. *This contribution presents some results of THM simulations with CODE_BRIGHT for two- and three-dimensional generic models of a nuclear waste repository in argillaceous host rock.*

1 INTRODUCTION

The deep geological disposal of high-level radioactive waste requires a prediction of the long-term behavior of a repository including (among others) thermal-hydraulic-mechanical (THM) coupled processes that must be considered in numerical simulations. It was the aim of the BenVaSim[i] project to investigate the basic processes, with special regard to flow processes, in simplified models of repository components to perform an international benchmarking for common THM simulators. Within the project, several one-dimensional repository models were considered at different levels of complexity. While the simulator results where in great accordance for the case of the HM modelling tasks, much larger differences in simulation results of different codes occurred for the considered THM problems due to different simulator frameworks. This observation led to the follow-up project BenVaSim II, which aims, on the one hand for an improved compilation of model assumptions for the one-dimensional problems considered in the first project phase, and, on the other hand to extend the benchmarking initiative to more complex, particularly two- and three-dimensional problems related to generic repository concepts. It is the aim of this contribution to present some the results that the authors obtained within the project by simulations performed with CODE_BRIGHT. Particularly, thermo-mechanical (TM) and thermo-hydraulic (TH) two-phase flow simulation results for a two-dimensional section through a waste canister and the surrounding backfill and host rock as well as TM simulations of a three-dimensional generalization are given and interpreted.

2 TWO-DIMENSIONAL MODEL WITH INCREASING PROCESS COUPLING COMPLEXITY

2.1 Model assumptions, conditions, and parameters

The two-dimensional model (Figure 1) describes a cross-section of a horizontal disposal drift considering canister and backfill as two different materials together with the surrounding argillaceous host rock. Prior to a fully coupled THM simulation, it is the aim to gradually increase the complexity of the problem. The different modeling steps are given by:

TM → TH (Richards) → TH (two-phase flow) → THM (Richards) → THM (two-phase flow)

Additionally, a variation of host rock material parameters from isotropic to transverse isotropic thermal (and mechanical) behavior is considered. Hereafter, the anisotropic TM and the isotropic TH (two-phase flow) problems are studied. For the TM problem, the energy balance, solid mass balance and stress equilibrium equations are solved. The constitutive assumptions are given by Fourier's law and linear elasticity with additional linear thermal expansion. A constant temperature of 28 °C is assumed at the top and bottom boundary and initially throughout the entire model. No heat flow is possible through the left and right boundary. The left, bottom and right boundary are mechanically fixed in normal direction and a vertical compressive total stress of 14 MPa is applied to the top boundary. The initial stress state is given by a compressive vertical total stress of 14 MPa and compressive horizontal total stresses of 10 MPa. A heat source distributed to the area of the canister is considered. The initial heat power of 51 W/m³ decreases linearly to zero within 1,000 years.

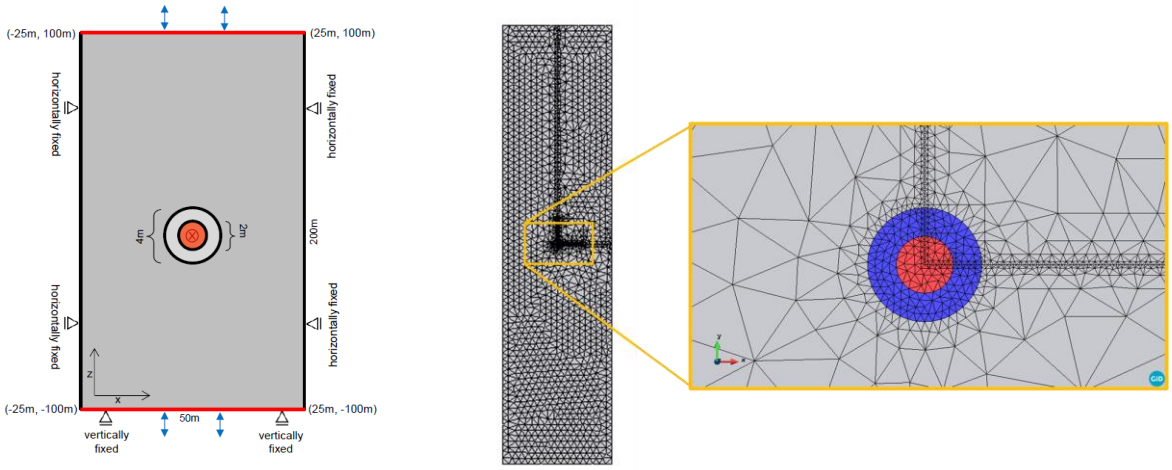


Figure 1: Model geometry and mesh details (2D model)

To tackle the TH (two-phase flow) problem, the energy, water mass, and gas mass balance equations are solved. The fluid phases follow Darcy's law with Mualem-van Genuchten relative permeability relations. The thermal boundary conditions and the heat source are identical to the conditions in the TM problem. No fluid flow is allowed through the left and right boundary. A constant fluid pressure of 0.1013 MPa is assumed for the top and bottom boundary and initially for the host rock. An initial liquid saturation of 0.2 and a gas pressure of 0.1013 MPa is given for the backfill. All parameters considered for the two-dimensional TM and TH problem are shown in Table 1.

2.2 Results

The results of the TM and TH simulations are given by the evolution of field quantities at different distances from the canister center along the horizontal and vertical symmetry axes and by profiles along these axes at different time instances. Temperature evolutions and displacement profiles for the TM simulation are given in Figure 2. The heat source generates a temperature increase during the first 200 years followed by a decrease to the initial temperature after 2,000 years. The temperature increase leads to a reversible expansion of the canister and the host rock while the backfill is being contracted. The assumption of thermo-elastic material behavior leads to a recovery of the initial mechanical state after the heat source has lapsed. The anisotropic thermal conductivity leads to a different temperature field in horizontal and vertical direction, see Figure 3.

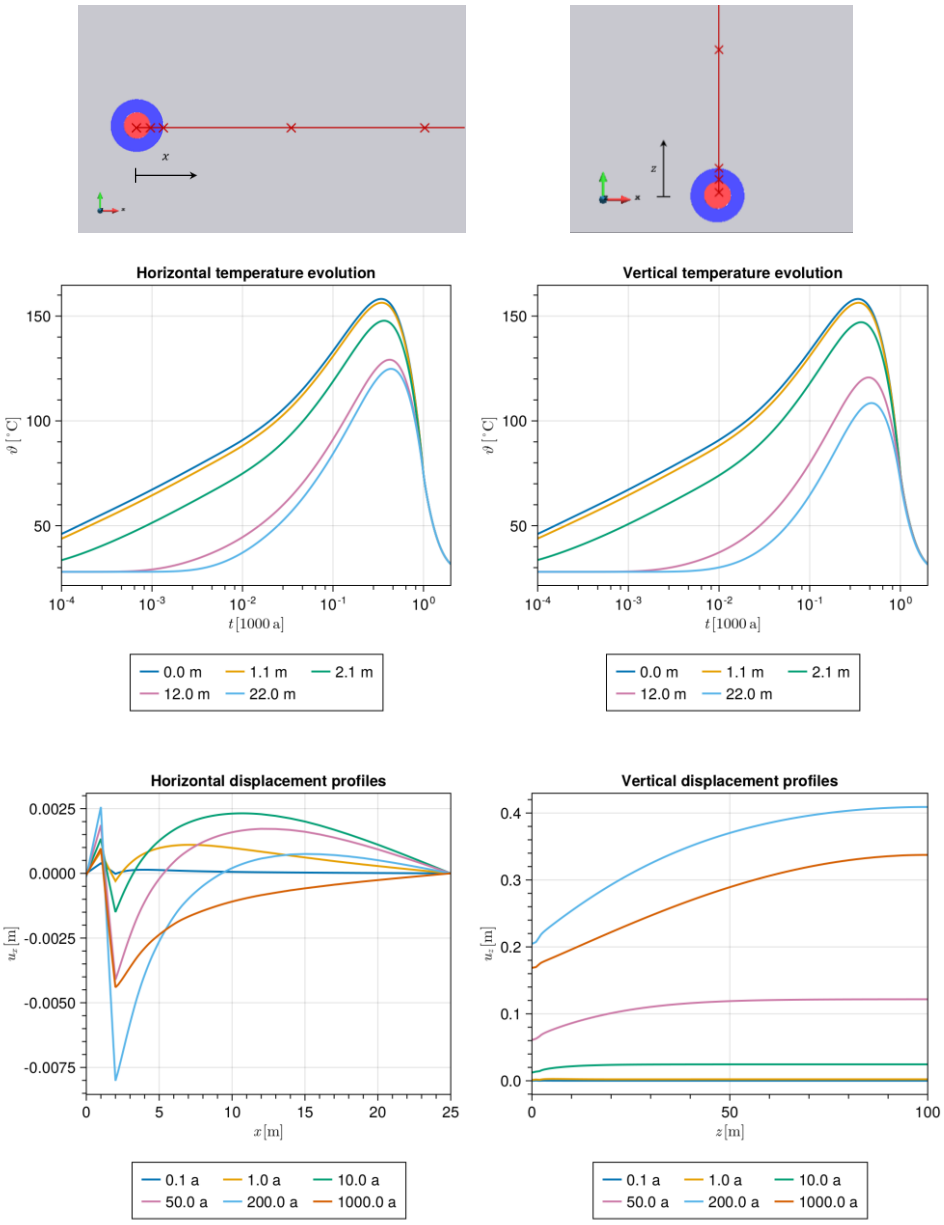


Figure 2: Horizontal and vertical evaluation points (top), temperature evolution (middle), and displacement profiles (bottom) for the TM simulation (2D model)

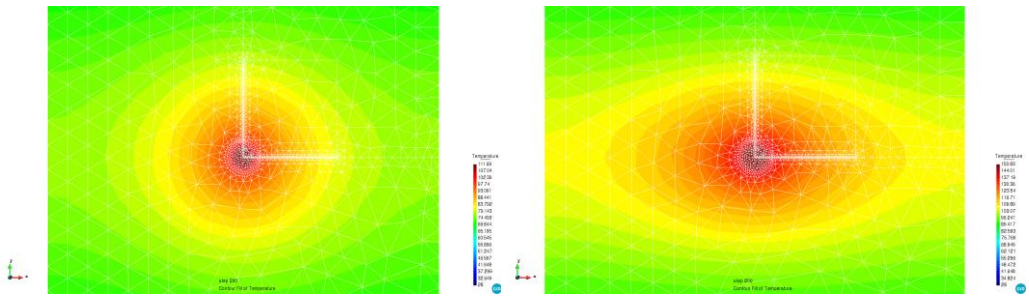


Figure 3: Temperature field for the TM simulation in case of an isotropic (left) and anisotropic (right) thermal conductivity (2D model)

solid phase properties	2D model (TM / TH)			3D model		
	canister	backfill	host rock	canister	backfill	host rock
general parameters						
specific density [kg/m³]	6,700	2,700	2,700	6,700	1,575	2,495
initial porosity [-]	0.01	0.45	0.12	0.01	0.45	0.12
thermal parameters						
horizontal thermal conductivity [W/(m K)]	16	2	1.75 / 2	16	2	2
vertical thermal conductivity [W/(m K)]	16	2	0.78 / 2	16	2	2
specific heat capacity [J/(kg K)]	500	900	900	500	900	900
linear elastic constitutive parameters						
horizontal Young's modulus [MPa]	195,000	100	10,000	195,000	100	5,000
vertical Young's modulus [MPa]	195,000	100	4,000	195,000	100	5,000
horizontal Poisson's ratio [-]	0.3	0.1	0.35	0.3	0.1	0.3
vertical Poisson's ratio [-]	0.3	0.1	0.25	0.3	0.1	0.3
shear modulus in vertical plain [MPa]	75,000	45	3,500	75,000	45	2,273
hydraulic parameters						
intrinsic permeability [m²]	1.0E-25	1.0E-16	1.E-20			
van Genuchten gas entry pressure [MPa]	0.1	10	10.9			
van Genuchten shape parameter [-]	0.5	0.4	0.29			
residual liquid saturation [-]	0	0	0.01			
residual gas saturation [-]	0	0	0			
coupling parameters						
lin. thermal expansion coefficient [1/K]	1.7E-5	2.5E-5	2E-5	1.7E-5	2.5E-5	2E-5
Biot coefficient [-]		1	0.8			

Table 1: Model parameters (2D and 3D model)

The liquid and gas pressure evolution and profiles for the TH simulation are given in Figure 4. The temperature evolution is similar as given in Figure 2 for the TM simulation. The temperature increase leads to a liquid pressure increase in the host rock in some distance from the drift contour and a short-term gas pressure build-up in and near the backfill. In this area, the host rock is slightly desaturated as it provides liquid for the backfill saturation. After full saturation has been reached in the backfill, a further liquid pressure increase occurs in the entire model as long as the temperature increases. The initial pressure is regained after the heat source has lapsed.

3 THREE-DIMENSIONAL GENERALIZATION AND TM SIMULATION

3.1 Model assumptions, conditions, and parameters

The three-dimensional generalization is derived from the two-dimensional model by adding a thickness (y-direction) of five meters comprising one half of a waste canister (2.5 m) and half the distance between two canisters (2.5 m), see Figure 5. The model approach is derived from the two-dimensional TM problem with the simplification of isotropic mechanical and thermal properties (Table 1).

3.2 Results

The results of the TM simulation are given by the temperature evolution and displacement profiles perpendicular to and along the canister axis (Figure 6). The graphs are in accordance with the observed behavior of the two-dimensional model. Particularly, reversible thermal expansion of canister and host rock combined with backfill contraction are shown.

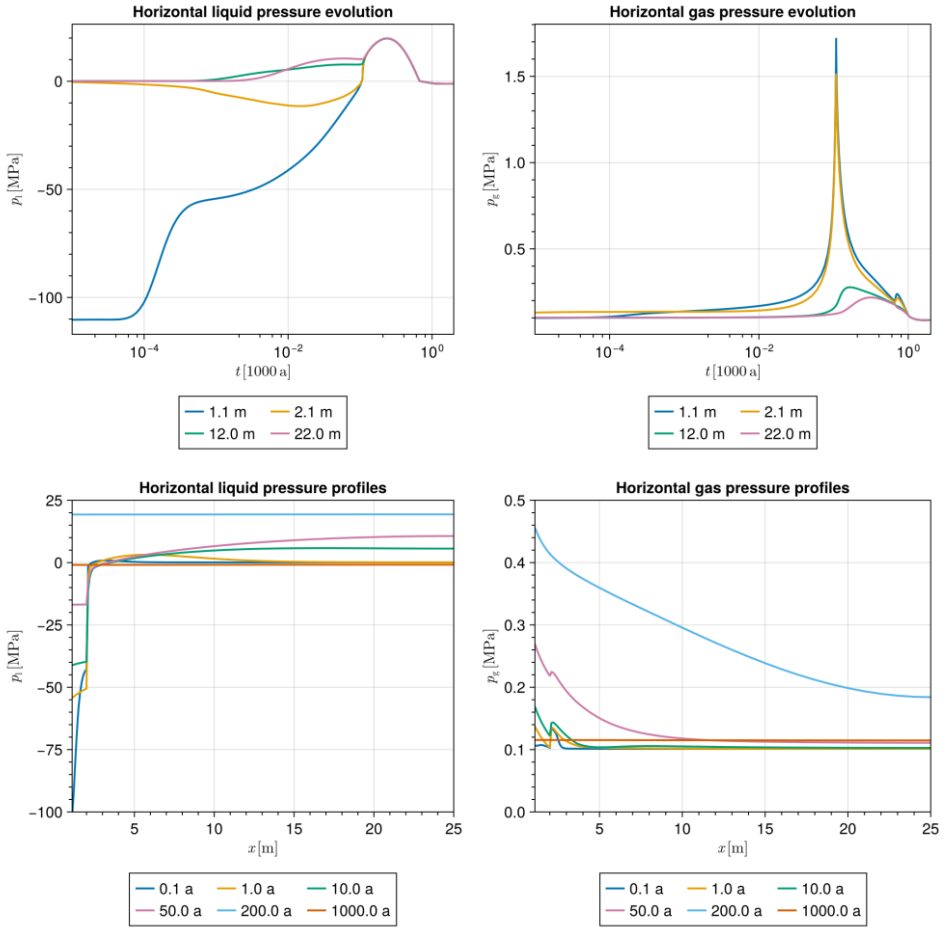


Figure 4: Evolution and profiles of liquid pressure for the TH simulation (2D model)

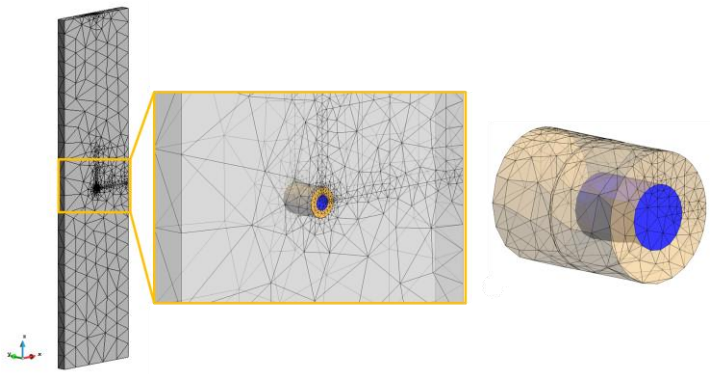


Figure 5: Model geometry and mesh details (3D model)

4 CONCLUSIONS AND OUTLOOK

The simulations of the considered two- and three-dimensional THM models of nuclear waste repository systems using CODE_BRIGHT show reasonable values of the computed field variables in space and time and particularly capture phenomena such as backfill saturation, host rock de- and resaturation, thermal expansion, thermal pressure increase and

anisotropy. The chosen model assumptions and parameters refer to a drift disposal concept in argillaceous host rock. However, not all model assumptions are intended to represent real conditions in a repository but to allow for a comparison of simulation results of different codes, which is the superior goal of the benchmarking project BenVaSim II.

The next step will be fully coupled THM simulations of the considered models and the introduction of more complex constitutive laws.

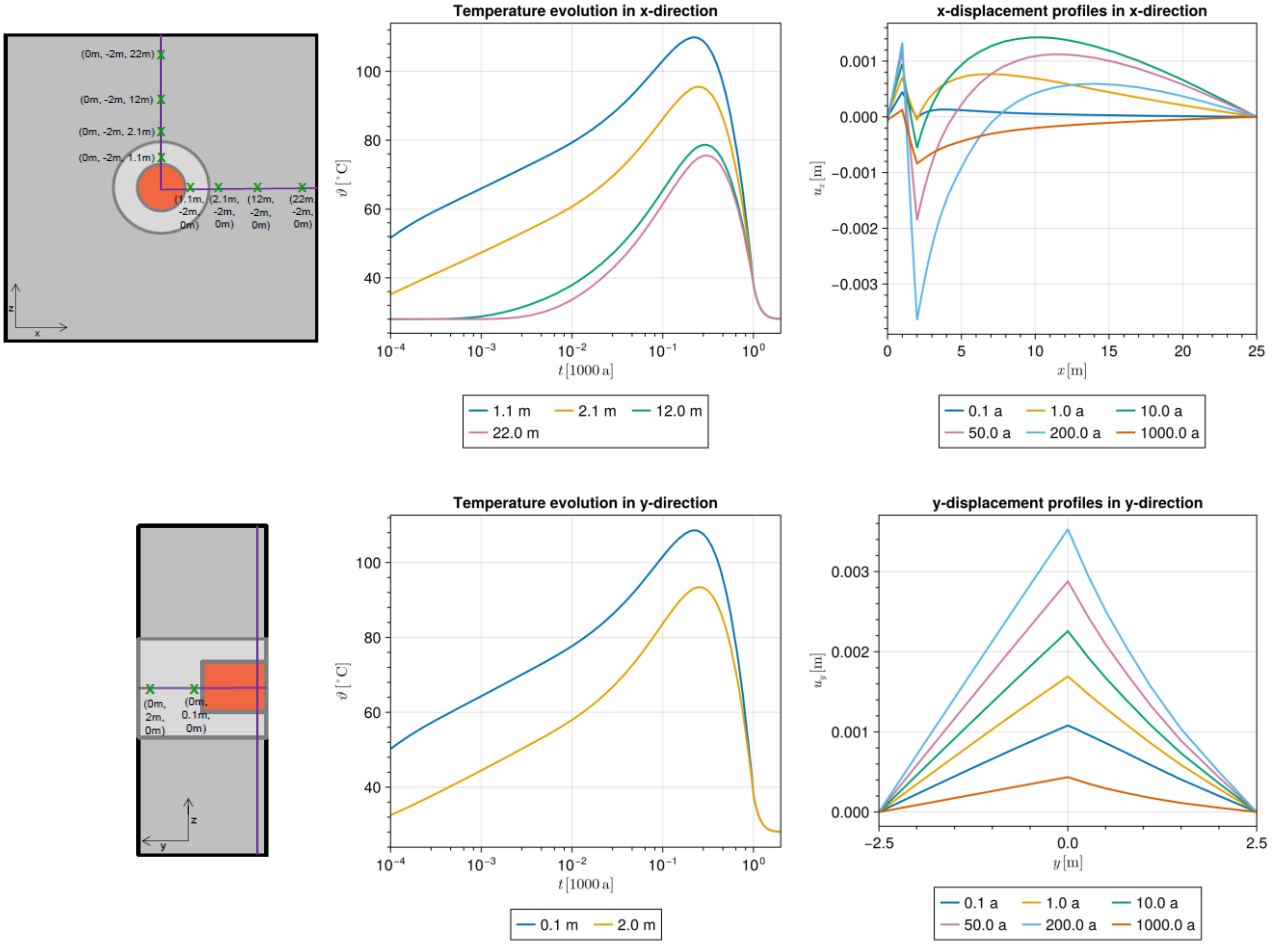


Figure 6: Temperature evolution and displacement profiles perpendicular to (top) and along (bottom) the canister axis for the TM simulation (3D model)

ACKNOWLEDGEMENTS

The project BenVaSim II is supported by the German Federal Ministry for the Environment, Climate Action, Nature Conservation and Nuclear Safety under contract 02E12022B.

REFERENCES

[i] Lux, K.-H., Rutenberg, M., Feierabend, J., Czaikowski, O., Friedenberg, L., Maßmann, J., Pitz, M., Sentis, M., Graupner, B., Hansmann, J., Hotzel, S., Kock, I., Rutqvist, J., Hu, M., Rinaldi, A.P. (2021) International Benchmarking for Verification and Validation of TH2M Simulators with Special Consideration of Fluid Dynamical Processes in Radioactive Waste Repository Systems (BenVaSim) Synthesis report. DOI: 10.13140/RG.2.2.28998.34887.

INSIGHTS INTO THE DAILY LIFE OF A NUMERICAL MODELER - AN EXEMPLARY CRUSHED SALT MODELING TASK -

Larissa Friedenberg

Gesellschaft für Anlagen- und Reaktorsicherheit (GRS) gGmbH
Braunschweig, 38122 Braunschweig, Germany
E-mail: larissa.friedenberg@grs.de

Key words: GiD interface, THM coupled analysis, Geological media

Abstract. *This paper is aimed to provide an insight into complexities of a crushed salt project related to repository research, especially with regard to modelling activities.*

1 PROJECT INTRODUCTION

Since 2018, an international initiative is striving to improve the process understanding of crushed salt compaction and permeability evolution in its entireness [i, ii, iii]. This knowledge is needed for the verification and validation of constitutive models that reliably predict the crushed salt performance for the long-term safety assessment of a HLW repository in rock salt.

The initiative's aim is to create a strong connection of crushed salt research from micro- to macro-scales and to foster an intensive exchange between experimental, microstructural and numerical studies. The ongoing progress helps to reduce uncertainties and therefore, improves the prognosis quality for the barrier properties of crushed salt.

In the first project phase of this initiative, methods and strategies were developed and an extensive experimental program was elaborated. Additionally, a reference material was specified that allows generic investigations on crushed salt. This material is permanently available and reproducible in its properties [i]. The second project phase focused on the application of the previously developed methods and strategies [ii]. Both project phases contributed highly to the increase in process understanding and strengthened the prognosis reliability of crushed salt compaction. Currently, a third phase is ongoing that addresses remaining open questions and newly appeared questions [iii].

One of the open questions is the effect of the laboratory which performs the compaction experiments and the comparability of experimental results between different labs. A subsequent question is the handling of common laboratory shortcomings in numerical simulations and how the modelers deal with the case of inconsistent experimental results. This paper is aimed to show some complexities in the handling of experimental data from modelers view.

2 COMPARABILITY OF EXPERIMENTAL DATA

2.1 Laboratory benchmark for crushed salt

A laboratory benchmark is performed to address the question of laboratory effects on experimental results. The basis for this benchmark builds the compaction test "TUC-V2" which combines the investigation of several influences on crushed salt compaction [ii]. TUC-V2 builds also the basis for calibration of constitutive models against the investigated dependences. Thus, a second aim of this benchmark is to examine if both tests can be modeled with one common parameter set.

For simplification, the first 150 days of the test are chosen for the benchmark only. They are characterized by various levels in mean stress and deviatoric load phases to investigate the influence of mean stress and deviatoric stress on the compaction behavior of crushed salt (Figure 1a). The test TK-044 is performed as benchmark test by a different lab (Figure 1b). The aim was to reproduce exactly the boundary conditions to ensure a temporal comparability. Both labs used the reference crushed salt material as specified in [i] and prepared samples with a water content of 0.5 w.-% and an initial porosity of around 17 %. However, each lab applied their own method for sample preparation that are documented in [i, ii].

After comparison of the experimental results, both tests are simulated with the parameter set calibrated for TUC-V2.

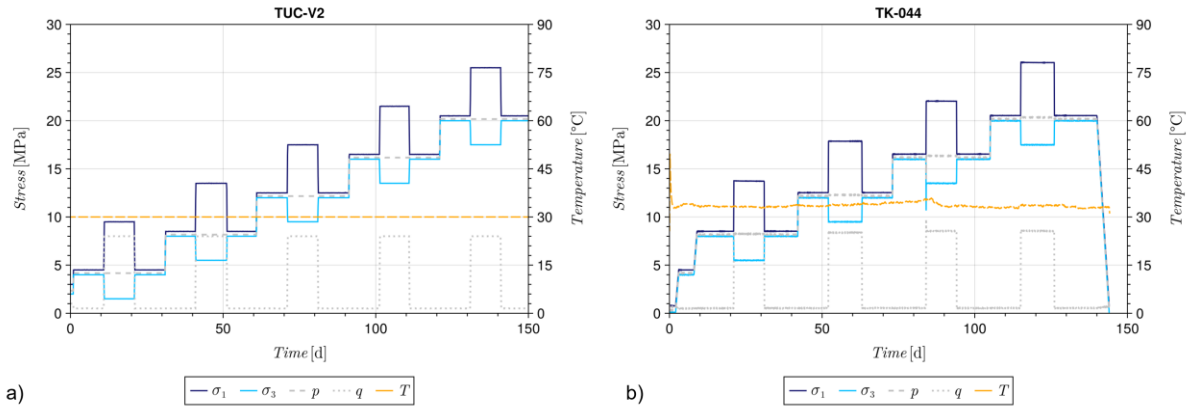


Figure 1: Boundary conditions for the triaxial compaction tests a) TUC-V2 (only 150 d) and b) TK-044. Modified after [ii]

2.1.1 Comparison of boundary conditions

The boundary conditions were well-defined in their value and temporal evolution due to the already existing data of TUC-V2. However, by comparing the evolutions for mean stress and deviatoric stress (Figure 2a and b) it is obvious that timing of stress increase as well as the duration of the stress phases differ between both tests. A direct temporal comparison of the measurement data is difficult. For the TUC-V2 test, temperature was well-controlled and kept constant over the test duration. For TK-044, in the beginning some increase of temperature to 50 °C can be recognized in the data. Afterwards, temperature was kept constant, but slightly higher than for TUC-V2.

From Figure 2a, the first challenge in performing a laboratory benchmark becomes obvious. The exact timing of boundary conditions and the adjustment of exact stress/temperature values strongly depends on the technical devices used and the technician who performs the tests.

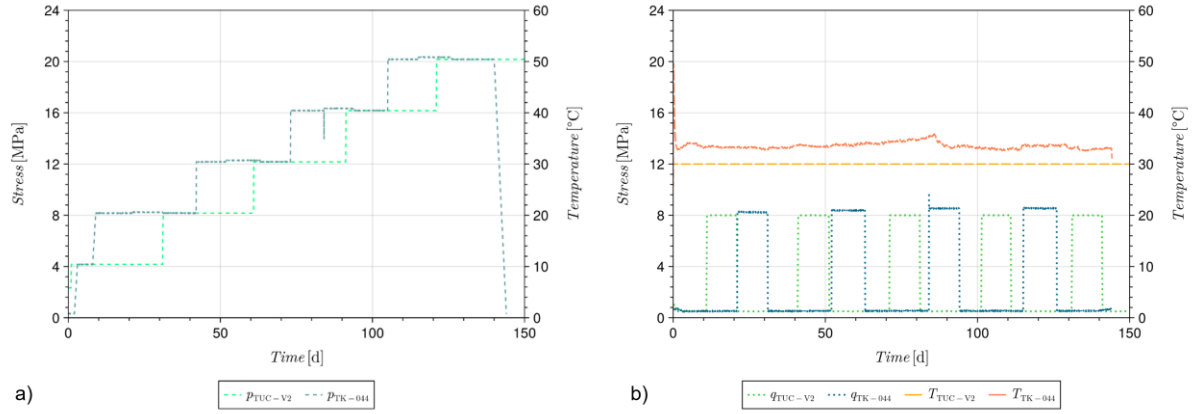


Figure 2: Comparison of boundary conditions for tests TUC-V2 and TK-044. a) Mean stress. b) Deviatoric stress and temperature

2.1.2 Comparison of experimental results

Figure 3 gives an overview of the comparison of experimental results for TUC-V2 and TK-044. More information is to be found in [2]. The comparison of volumetric strain and axial strain is shown in Figure 3a. These two quantities are chosen, since they are directly measured in the test by determining the axial and volumetric deformation. Not only the final compaction state of both samples is different, but also the evolution. In the beginning of TUC-V2, the axial strain is higher than the volumetric strain. This switches around 90 days and volumetric compaction becomes lager. For TK-044, volumetric strain is higher than axial strain for the whole duration of the test. This observation can be explained by the different sample preparations. The sample for TUC-V2 was radially pre-compacted, whereas the sample for TK-044 was pre-compacted axially.

Thus, the large difference in the volumetric compaction is still an open question and might be related to microstructural effects.

Figure 3b shows the relation between volumetric strain rate and porosity for both tests. The comparability is poor, both tests show completely different behaviors.

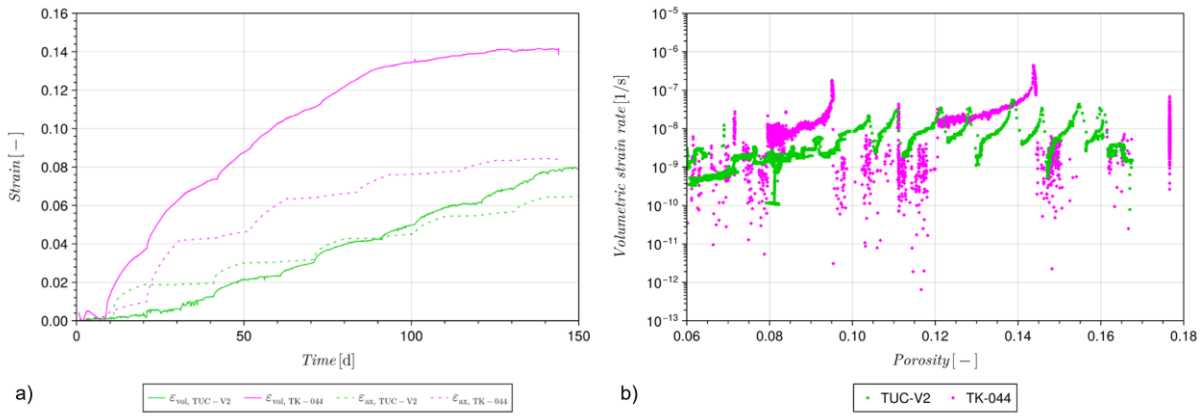


Figure 3: Comparison of experimental data for TUC-V2 and TK-044. a) Volumetric and axial strain vs time. b) Volumetric strain rate vs porosity

2.1.3 Conclusion for the laboratory benchmark

The laboratory benchmark as presented above shows clear differences between the tests TUC-V2 and TK-044 in the comparison of temporal evolution for strains, in the value of compaction, especially for volumetric strain, and in the comparison of the relationship between mean stress and compaction.

Differences are figured out due to the influence of the lab itself (technical devices, laboratory staff) and the individual pre-compaction methods that lead to microstructural differences in the samples. Possible reasons which may have an additional effect lie in the measurement systems and related measurement uncertainties, especially, for low porosities [ii].

All in all, the laboratory benchmark raised more questions than it could answer. But what does it mean for the numerical modeling? Two tests with the same boundary conditions are performed and gain different results. Is there a "correct" test and an "incorrect" test? Is the data valuable? How can we handle the different pre-treatments of the sample? How to include the lab uncertainties in the model? For clarification of these questions and more which are not mentioned, it needs an intensive exchange with the experimental experts.

2.2 Correlation of mean stress dependences

In the frame of the second project phase, another triaxial compaction test was performed after TK-044 by the respective lab, addressing only the influence of mean stress on compaction. This test, TK-045, is performed with mean stress levels comparable to the TUC-V2 set-up to allow for comparability.

Figure 4 shows the stress and temperature boundary conditions for TUC-V2 in its entireness and TK-045. Again, the comparison includes two labs, and two samples prepared with different pre-compaction methods, but for nearly equal starting conditions ($w = 0.5$ w.-%, $\Phi_{TUC\text{-}V2} = 0.165$, $\Phi_{TUC\text{-}V2} = 0.13$).

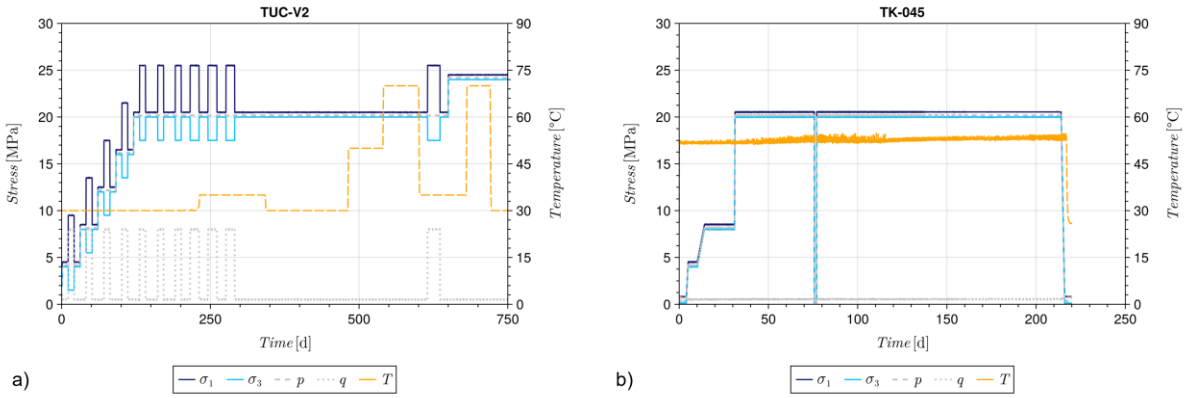


Figure 4: Boundary conditions for a) TUC-V2 and b) TK-045

The experimental results for TUC-V2 and TK-045 are compared in Figure 5. For the comparison of volumetric strain evolution over time, the TK-044 data is added (Figure 5a). Even if TK-045 was exposed to higher mean stress and a longer duration of compaction, its final volumetric strain is much lower than for the TK-044 sample. The final value for compaction of TK-044 is about the same as for TUC-V2, however, there is a big difference in time. Comparing the evolutions for TUC-V2 and TK-045 there is no accordance visible.

Considering the volumetric strain rate versus porosity good accordance between the test is

observed for a porosity between 12 and 13 % and between 5 and 7 % (Figure 5b).

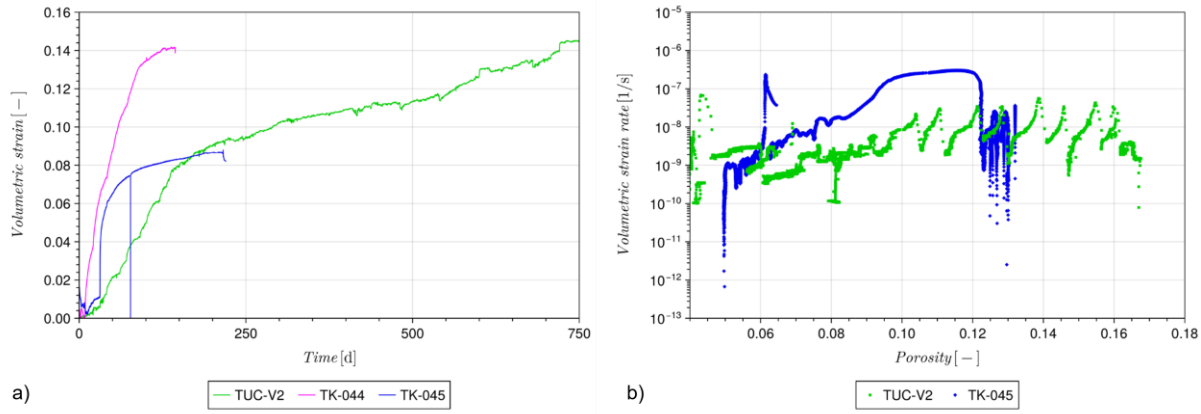


Figure 5: Comparison of experimental data. a) Volumetric strain vs time for TUC-V2, TK-044 and TK-045. b) Volumetric strain rate vs porosity for TUC-V2 and TK-045

In the comparison of TUC-V2 and TK-044, big differences are observed. Test TK-045 was performed in the same lab as TK-044 and the sample produced with the same pre-compaction treatment (which differs from the TUC-V2 one). Nevertheless, the experimental data shows a better comparability with TUC-V2.

3 NUMERICAL MODELING OF CRUSHED SALT COMPACTION TESTS

3.1 Basics

For the numerical simulation of crushed salt compaction with CODE_BRIGHT, the available mechanical constitutive model is applied:

$$\dot{\varepsilon} = \dot{\varepsilon}_{EL} + \dot{\varepsilon}_{FADT} + \dot{\varepsilon}_{DC} + \dot{\varepsilon}_{VP} \quad (1)$$

It is described by an additive approach of various mechanisms: linear elastic deformations (EL), fluid assisted diffusional transfer mechanism (FADT), dislocation creep (DC) and viscoplastic deformations (VP). The governing equations and detailed descriptions can be found in [iv].

The hydraulic behavior is modeled as one-phase flow with a constant gas pressure of 0.1 MPa.

All simulations shown below are performed using the “TUC-V2 parameter set” determined by calibrating the model against the TUC-V2 test. The calibration procedure is described in [i, ii]. Figure 6 shows the simulation of the TUC-V2 test with the final calibrated parameter set.

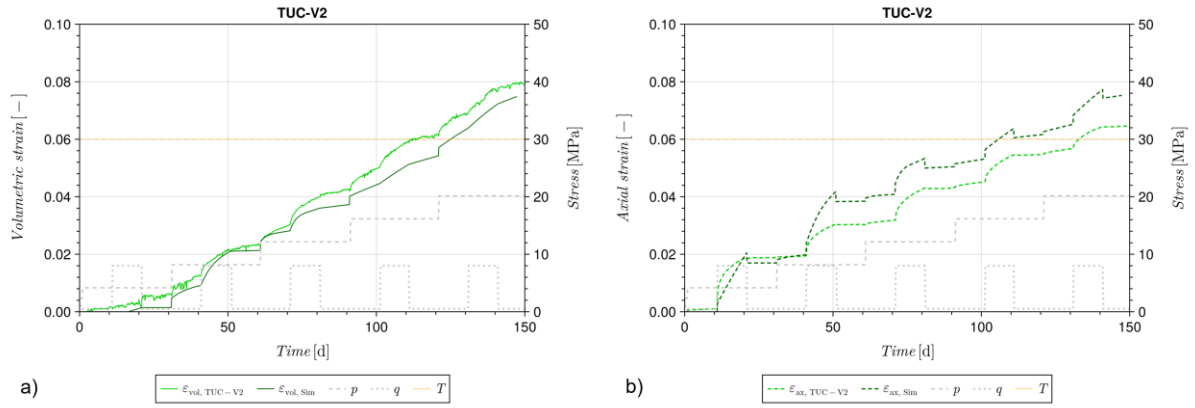


Figure 6: Experimental data vs. simulation for TUC-V2. a) Volumetric strain. b) Axial strain.

The accordance between the numerical results and the experimental data is satisfactory.

Due to the disagreement in the experimental data between TUC-V2 and TK-044 it is obvious that the results of TK-044 could not be reproduced with the "TUC-V2 parameter set".

3.2 Modeling of TK-045 with the "TUC-V2 parameter set"

The comparison of experimental data of TUC-V2 and TK-045 show some good accordance in the relationships with respect to mean stress. Thus, test TK-045 was simulated using the "TUC-V2 parameter set". Figure 7 shows the comparison of experimental data with numerical results. A very good accordance is achieved with the "TUC-V2 parameter set" that leads to the conclusion of a correct correlation of mean stress and compaction in the constitutive model.

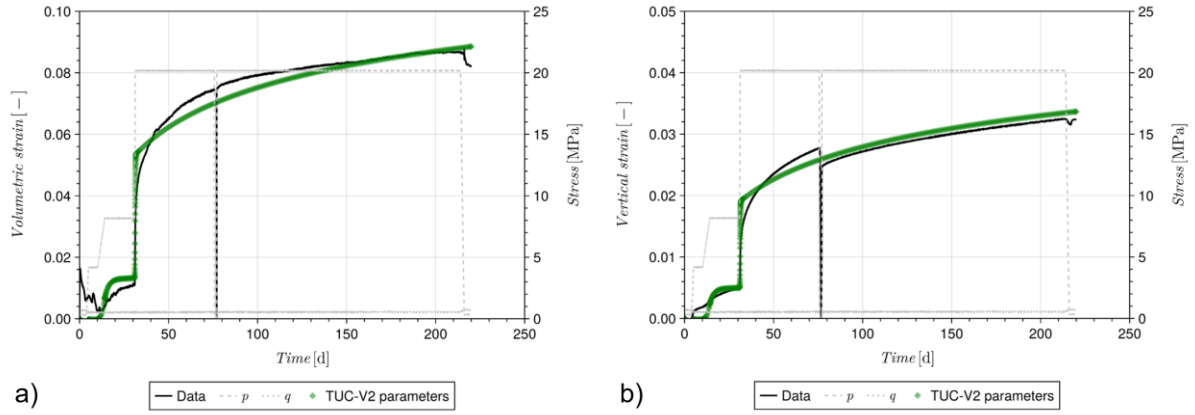


Figure 7: Experimental data vs. simulation TK-045. a) Volumetric strain. b) Axial strain.

The numerical results raise some questions. The pre-compaction method is meant to play a major role for the compaction behavior of the crushed salt samples. However, Figure 7 shows that there is no need to adapt the parameter set for the pre-compaction method to achieve a good accordance. Further, there seems not to be a major influence of the lab. As a modeler, the results in Figure 7 are quite successful, however, one should not forget to see the whole picture and question the own numerical results constantly.

4 CONCLUSIONS & LESSONS LEARNED

This paper aims to give an insight into complexities that may occur during research projects and their effect on numerical modeling. Examples are shown from an international crushed salt project.

Lessons learned for a numerical modeler can be summarized in four points:

- Understand the physics behind the experiments.
- Study the input data and question the performance.
- Always check your results.
- Communicate with other disciplines, especially, with the persons who produced the input data.

REFERENCES

[i] Czaikowski, O., Friedenberg, L., Wieczorek, K., Müller-Hoeppe, N., Lerch, C., Eickemeier, R., Laurich, B., Liu, W., Stührenberg, D., Svensson, K., Zemke, K., Lüdeling, C., Popp, T., Bean, J., Mills, M. M., Reedlunn, B., Düsterloh, U., Lerche, S., & Zhao, J. (08/2020). Kompass: Compaction of crushed salt for the safe containment (GRS-608). Gesellschaft für Anlagen- und Reaktorsicherheit (GRS) gGmbH.

[ii] Friedenberg, L., Bartol, J., Bean, J., Beese, S., Bresser, H. J. P. de, Coulibaly, J. B., Czaikowski, O., Düsterloh, U., Eickemeier, R., Gartzke, A.-K., Hangx, S., Jantschik, K., Laurich, B., Lerch, C., Lerche, S., Liu, W., Lüdeling, C., Mills, M. M., Müller-Hoeppe, N., . . . Zemke, K. (January 2024). Kompass-II: Compaction of Crushed Salt for Safe Containment - Phase 2 (GRS-751). Gesellschaft für Anlagen- und Reaktorsicherheit (GRS) gGmbH.

[iii] Friedenberg, L., Bartol, J., Beese, S., Coulibaly, J. B., Düsterloh, U., Gartzke, A.-K., Hangx, S., Jantschik, K., Kirby, M., Laurich, B., Lerch, C., Lerche, S., Li, L., Lüdeling, C., Mills, M. M., Naumann, D., Norris, S., Oosterhout, B. van, Rahmig, M., . . . Zemke, K. (2025). Multi-Scale Experimental and Numerical Analysis of Crushed Salt Used as Engineered Backfill in a Rock Salt Repository - 25062. In I. N. WM SYMPOSIA (Chair), Waste Management Symposia 2025, Phoenix.

[iv] Olivella, S., Gens, A. 2002. A constitutive model for crushed salt. International Journal for Numerical and Analytical Methods in Geomechanics, 26(7), 719–746. https://doi.org/10.1002/nag.220